



**HAL**  
open science

## Spectroscopic autoradiography of alpha particles using a parallel ionization multiplier gaseous detector

Hugo Lefeuvre, Jérôme Donnard, Michael Descostes, Sophie Billon, Samuel Duval, Tugdual Oger, Hervé Toubon, Paul Sardini

► **To cite this version:**

Hugo Lefeuvre, Jérôme Donnard, Michael Descostes, Sophie Billon, Samuel Duval, et al.. Spectroscopic autoradiography of alpha particles using a parallel ionization multiplier gaseous detector. Nuclear Instruments and Methods in Physics Research Section A: Accelerators, Spectrometers, Detectors and Associated Equipment, 2022, 1035, pp.166807. 10.1016/j.nima.2022.166807 . hal-04392796

**HAL Id: hal-04392796**

**<https://hal.science/hal-04392796>**

Submitted on 22 Jul 2024

**HAL** is a multi-disciplinary open access archive for the deposit and dissemination of scientific research documents, whether they are published or not. The documents may come from teaching and research institutions in France or abroad, or from public or private research centers.

L'archive ouverte pluridisciplinaire **HAL**, est destinée au dépôt et à la diffusion de documents scientifiques de niveau recherche, publiés ou non, émanant des établissements d'enseignement et de recherche français ou étrangers, des laboratoires publics ou privés.



Distributed under a Creative Commons Attribution - NonCommercial 4.0 International License

1 **Title page**

2

3 Spectroscopic autoradiography of alpha particles using a parallel ionization multiplier gaseous  
4 detector

5

6 **Coauthors:**

7 Hugo LEFEUVRE<sup>a, b, \*</sup>, Jérôme DONNARD<sup>c</sup>, Michael DESCOSTES<sup>d, e</sup>, Sophie BILLON<sup>b</sup>, Samuel  
8 DUVAL<sup>c</sup>, Tugdual OGER<sup>c</sup>, Hervé TOUBON<sup>d</sup>, Paul SARDIN<sup>b</sup>

9

10 **Affiliations:**

11 <sup>a</sup> ERM (SARL), 7 rue Albert Turpain, 86000, Poitiers, France

12 <sup>b</sup> IC2MP – HydrASA, Poitiers University UMR 7285 CNRS, France

13 <sup>c</sup> AI4R (SAS), 2 rue Alfred Kastler, Nantes, France

14 <sup>d</sup> ORANO Mining, R&D Dpt, 125 Av. de Paris, 92320 Châtillon, Paris, France

15 <sup>e</sup> Centre de Géosciences, MINES ParisTech, PSL University, 77300 Fontainebleau, France.

16

17 Corresponding author: Hugo LEFEUVRE\*

18 E-mail address: hugo.lefeuvre@univ-poitiers.fr

19 Postal address: IC2MP - UMR 7285, B27, 4 RUE MICHEL BRUNET, TSA 51106 ,86073 POITIERS,  
20 Cedex 9, France.

21 **Abstract:**

22 Geoscience is a field of study where nuclear instruments find their place for conducting specific  
23 measurements of radioactivity, usually to improve the monitoring of natural processes using naturally-  
24 occurring radioactive tracers, but also for the nuclear industry linked to the mining sector. In geological  
25 samples, the location and identification of the minerals bearing radioactivity at the thin-section scale  
26 remains a major challenge as the detection limit of the usual elementary microprobe techniques is far  
27 higher than the concentration of most of the natural radioactive decay products. The location of each  
28 decay product, as in the case of uranium-238 series in a geomaterial is interesting for relating  
29 radionuclide concentrations to mineralogy. The present study aims to provide spectroscopic  
30 autoradiography analysis method for measuring the initial energy of alpha particles with a parallel  
31 ionization multiplier gaseous detector. This spectroscopic autoradiography method was successfully  
32 used to reproduce the alpha spectra from a  $^{238}\text{U}$  decay chain on a geological sample at the thin-section  
33 scale. The characteristics of this measurement are an energy spectrum resolution of 17.2% (FWHM) at  
34 4647 keV and a spatial resolution of at least 50  $\mu\text{m}$ . Even if the efficiency of energy spectrum  
35 reconstruction is low (4.4%) compared to the efficiency of a simple autoradiograph (50%), this novel  
36 measurement approach offers the opportunity to select areas on an autoradiograph to perform an energy  
37 spectrum analysis within that area. This opens up possibilities for the detailed analysis of heterogeneous  
38 geological samples containing natural alpha emitters such as uranium-238 and radium-226.

39  
40  
41  
42

43 **Keywords:** Alpha particles; Digital autoradiography; Alpha spectroscopy; Uranium decay products;  
44 Mining activities; Parallel ionization multiplier.

45

## 46 **1 Introduction**

47 Autoradiography [1] is a non-destructive imaging method for studying and locating in two dimensions  
48 the radioactivity emanating from a surface sample, at scales ranging from hectometer to micrometer [2].  
49 The distinctiveness of autoradiography is based on the fact that the source is the object itself.  
50 Radioactivity imaging is performed using a detector which integrates and spatializes the radioactive  
51 emissions during a given acquisition time. The image definition is closely related to the choice of sensor.  
52 Film autoradiography (FA) using a silver-bromide emulsion was the first technique employed [3]. It is  
53 still widely used because of its low cost and very good spatial resolution (about 10  $\mu\text{m}$ ). To reveal the  
54 signal information, the film must be digitized. Advances in autoradiograph technology now makes it  
55 possible both to digitize the activity map directly and to observe the signal accumulation in real time.  
56 Autoradiography is well suited for use in the life and earth sciences. Thin sections of radiolabelled  
57 animal organs mounted on microscope glass slides are conventionally imaged by autoradiography. *Ex*  
58 *vivo* autoradiography is used by biologists as a complementary tool in positron emission tomography  
59 (PET) [4][5], for instance to better understand drug effects or degenerative diseases. Applications of  
60 autoradiography for geosciences include, among others, the characterisation of pore space and transport  
61 properties of rocks [6][7][8], and the distribution of natural disintegration series in rocks [9].

62 In that context, the study of autoradiography use for alpha particle characterisation is increasing in the  
63 geosciences. The present contribution is focused on the study of the natural series found in geo-materials  
64 (rocks or U mill tailings). A lot of devices have been developed for imaging the emission of alpha  
65 particles. The traditional method uses a solid-state nuclear track detector (SSNTD). SSNTD is a  
66 medium, typically a polycarbonate film, in which the passage of an ionizing particle leaves a latent track  
67 that can be made visible by an appropriate chemical treatment. Depending on the track size, the  
68 observation can be performed with the naked eye, using an optical microscope or a scanning electron  
69 microscope (SEM). For further details the reader can refer to applications in geosciences [10][11][12]  
70 and also in biology [13]. Phosphor screens autoradiography (PSA) is an alternative method using  
71 reusable films, that used to be employed for imaging the ppm of U and Th in geo-materials [14]. The  
72 detection of particles is based on the property of phosphorescence. The energy imparted by incident  
73 radiation (light, X-rays, gamma rays, alpha or beta particles) is temporarily stored by the excited atoms  
74 in a photostimulable phosphor plate based on BaFBr:  $\text{Eu}^{2+}$ . Then, de-excitation can be induced by laser  
75 scanning to stimulate characteristic emissions of photons that are interpreted to form an image. All  
76 autoradiograph techniques of alpha particles described above store information in films. The sample  
77 exposure time can only be estimated, so there is a high risk of overexposure or underexposure.  
78 Nowadays, real-time autoradiography is becoming increasingly favored. The advantages of this  
79 approach are the direct counting of the emissions, the direct digitization of the image in a raster file, and  
80 the real-time acquisition. The first application of real-time autoradiographs was in the field of medicine.  
81 The “ $\alpha$ -Camera”, used in alpha-therapy, was developed using a scintillator and a CCD camera [15][16]  
82 with detector area about 5 x 5  $\text{cm}^2$ . The iQID system [21], which uses a similar technology to the  $\alpha$ -

83 Camera, is described in [22]; the detector area can be 4 cm or 12.5 cm diameter. This device has  
84 applications in pre-clinical and clinical scintigraphy [23]. For radiotherapy, the Timepix chip based on  
85 a pixelized semi-conductor is used for alpha particle autoradiography with 14 x 14 mm<sup>2</sup> area [17][18].  
86 First developed for biological applications such as alpha-therapy (using <sup>223</sup>Ra) [19][20], the BeaQuant  
87 system also created the first alpha autoradiograph of a geological thin section [24]. This technology is  
88 based on a gaseous detector incorporating micromesh Parallel Ionization Multiplier (PIM) [25][26][27]  
89 which allows the detection of both alpha and beta particles, together or separately. Alpha  
90 autoradiography using this detector is considered to be not disturbed by beta particles when used in the  
91 alpha imaging mode. The special feature of this autoradiograph is its large detection surface (up to 20 x  
92 20 cm<sup>2</sup>) in comparison with other real-time autoradiograph. It has a good spatial resolution (<50 μm for  
93 alpha and 20 μm for beta particles, mainly because the charge distribution is different), and is insensitive  
94 to X-Ray and gamma. The linearity of the detector reaches five orders of magnitude. The maximal  
95 acceptable counting rate over the whole analysed area is 20 × 10<sup>3</sup> cps (counts per second), and the  
96 background level for alpha counting is in the order of 6.3 × 10<sup>-4</sup> cps/mm<sup>2</sup>. The efficiency for alpha  
97 particle detection is 50% according to Billon, et al., 2019 [28].

98 Concurrently, spectroscopic autoradiography (called SA) is performed by simultaneously combining  
99 autoradiography with a spectral measurement. For alpha particles, different types of detector  
100 technologies make this dual measurement possible. But there is often a trade-off between spatial  
101 resolution, energy resolution and the field of view.

102 SSNTD can be used as a basic SA, by analysing the size distribution of the alpha tracks [29] [30]. A  
103 previous study employing SSNTD demonstrated an energy resolution optimised at around 2% FWHM  
104 [31] by using the range property of alpha particles. The application is however limited when alpha tracks  
105 are overlaid on each other, if the activity is too high or if the exposure time is too long.

106 A scintillator coupled to a silicon photomultiplier array allows the measurement of the particles' energy  
107 and emission point. For instance, in [32], the plutonium found around Fukushima has been studied by  
108 spectroscopy allowing the separation of alpha and beta particles. The energy resolution was good, but  
109 the spatial resolution (of 600 μm FWHM) was not suitable for high resolution autoradiography  
110 applications because of the limited pixelisation (64 channels over a 26 x 26 mm<sup>2</sup> detection area).

111 As an alternative to SiPM, a demonstration using an organic scintillator (stilbene) coupled to a 8 x 8  
112 position-sensitive photomultiplier tube (PS-PMT) [33] gave an energy resolution of 21.6% FWHM for  
113 <sup>241</sup>Am.

114 Using Timepix [34] for counting and the alpha spectrometer modes to identify and quantify radon and  
115 thorium gave an energy resolution of 2.3% for <sup>241</sup>Am (α-decay energies are 5.486 MeV). Following  
116 further calibration in the alpha mode, the energy resolution is 0.7% FWHM [35][36]. However, in terms

117 of imaging, the restricted detection area of 14 x 14 mm<sup>2</sup> makes the use of this method impractical for  
118 large samples. The spatial resolution can reach 18 μm [37] for alpha particles.

119 According to [38], the iQID device can locate and determine the energy of individual particles, with  
120 sufficient energy resolution to distinguish between different particle types (fission fragment, β, and α  
121 decay). However, using a ZnS(Ag) scintillator the expected energy resolution would not be better than  
122 40% FWHM at 5.5 MeV according to reference [39][45].

123 The radiobiology application of the fluorescent nuclear track detector (FNTD) has demonstrated its  
124 ability to visualise individual alpha particles and simultaneously measure their position, trajectory  
125 direction and energy with good accuracy [40]. However, the detection area is limited (100 x 100 μm<sup>2</sup>)  
126 and the energy resolution is 11.8% FWHM for an <sup>241</sup>Am source according to [41].

127 In the field of gaseous detectors, despite the possibility of having a good energy resolution [42][43],  
128 there are few instruments that can combine imaging and energy measurement. For example, a 31 cm  
129 thick time projection chamber using CF<sub>4</sub> showed an energy resolution of 6.7% (K = 1) at 5.3 MeV, and  
130 a spatial resolution of 6.8 mm [44]. The latter detector has been used to measure radioactive impurities  
131 of <sup>238</sup>U and <sup>232</sup>Th in low activity samples. The resolutions of different technologies are summarized in  
132 Table 1.

133 In order to meet the needs of the analysis of radioactive geological samples (pluri-centimetric sample  
134 and good spatial resolution), this study examines the possibility of combining the spatial and energy  
135 measurement of emitted alpha particles using the BeaQuant system. Our objective is to evaluate the  
136 possibility of obtaining the energy spectrum of alpha particles, with the final aim of spatializing the  
137 energy distribution on the autoradiograph. This, in order to better characterize the distribution of natural  
138 decay products (notably the <sup>238</sup>U series) that can be found in geomaterials [46][47][48]. Examples for  
139 <sup>238</sup>U series are provided.

## 140 **2 Alpha SA method using a parallel ionization multiplier**

141 Originally, the used detector was developed and optimized for beta particle autoradiography [25].  
142 Because alpha and beta particles do not interact in the same way with the detector, a simulation model  
143 was performed with the Geant4 toolkit in order to understand and interpret the data measured. Alphas  
144 deposit more energy than betas per unit path length and have a quasi-straight trajectory. Knowledge of  
145 the particles' position and energy along their trajectory through the detector is crucial for developing a  
146 spectroscopy method.

### 147 **2.1 Sample material and the PIM detector characteristics**

148

### 149 **2.1.1 Characteristics of a geological sample emission spectrum**

150 Determining the alpha emission energy spectra using the PIM is our main goal. Let  $E_0$  be the emission  
151 energy of an alpha particle when leaving the source/sample and penetrating the gas medium.  $E_0$  is  
152 influenced by the self-absorption and the loss of energy in interaction with the source media before the  
153 arrival in the detector gas media. Then, the emission energy spectrum of alphas can be modified by the  
154 source geometry (thickness) and nature (density). Three examples of spectra obtained with the AASI  
155 simulation program [49] are shown in Supplementary Material, Figure S1. Note that a source is named  
156 as “thin source” if its thickness can be neglected with respect to the mean range of the alpha particles  
157 propagating into it, and “thick source” otherwise. The red spectrum corresponds to a  $0.018\ \mu\text{m}$  ( $9\ \text{g}/\text{cm}^3$ )  
158  $5485\ \text{keV}$  mono-energetic  $^{241}\text{Am}$  alpha source. The blue one corresponds to the same emitter but in a  $9\ \mu\text{m}$   
159 ( $9\ \text{g}/\text{cm}^3$ ) thick source characterized by a staircase shape falling at  $5485\ \text{keV}$ . The third spectrum (in  
160 green), resulting from a multi-alpha  $9\ \mu\text{m}$  thick source ( $9\ \text{g}/\text{cm}^3$ , the same as the blue spectrum),  
161 illustrates the case of a “real” geological sample containing the 8 alpha emitters isotopes from the decay  
162 chain of  $^{238}\text{U}$  at secular equilibrium. One can appreciate the complexity of the spectroscopic approach  
163 applied to geological samples. Indeed, they are often in the form of materials of about  $30\ \mu\text{m}$  thick on a  
164 thin section, and may exhibit the three natural decay chains ( $^{238}\text{U}$ ,  $^{235}\text{U}$  and  $^{232}\text{Th}$ ) in which the most  
165 energetic alphas emitting from  $^{214}\text{Po}$  ( $7686\ \text{keV}$ ) have an average internal range of  $20$  to  $40\ \mu\text{m}$ . This  
166 range combined with usual thickness of the sample means that there is considerable self-absorption and  
167 energy loss.

### 168 **2.1.2 PIM detector description and charge readout**

169 The detector structure used for this study is schematized in Figure 1. The active part of the detector is a  
170 volume of gas segmented into three zones by two thin micromeshes that are sandwiched between a  
171 cathode and an anode. The cathode of the detector is the sample itself, which is mounted on a microscope  
172 slide and preferably coated with a conducting layer. The gap of  $400\ \mu\text{m}$  between the sample and the first  
173 micromesh is achieved with a spacer machined with FR-4 material. This gap creates the first  
174 amplification space (of gain  $G_1$ ), placed directly in contact with the sample. The second zone of  $1\ \text{cm}$   
175 thickness is a drift space used to propagate the electron cloud. It is defined by the space between the two  
176 micromeshes. Finally, the space between the second micromesh and the segmented anode defines the  
177 third zone, which is a second amplification stage (of gain  $G_2$ ).

178 An alpha particle coming from the sample interacts with the gas and generates electron-ion pairs by  
179 ionization of the gas atoms along its rectilinear-like path. The number of primary electrons  
180 ( $\text{nb}_{\text{primary\_charge}}$ ) is proportional to the raw energy deposited ( $E_{\text{dep}}$ ) by the alpha particle in the detector.  
181 The electrons created will be multiplied and collected on the segmented reading anode. The induced  
182 currents generated by the charge drift in the amplification space 2 are measured by application-specific  
183 integrated circuits (ASICs).

184 The intensity of the signal measured is more intense at the position where the alpha particles first ionize  
185 the gas (black colour in amplification space 2, Figure 1), than the intensity measured from the  
186 interactions in the drift space (dark blue in amplification space 2). The two histograms representing the  
187 charge of the collected electrons (called “charge histograms”) are recorded for each event along the X  
188 and Y axes. The initial position of the alpha particles, the energy deposited in the detector and the  
189 projected X and Y distances of the trace are estimated thanks to these charge histograms. Unlike  
190 calorimeters, since not all particles stop in the gas, the deposited energy is not directly proportional to  
191 the emission energy  $E_0$ .

## 192 **2.2 Simulation of the alpha emission interaction in PIM with Geant4**

193

### 194 **2.2.1 Behavior of alpha particles interacting with the detector**

195 The PIM detector and the alpha tracks modelled with Geant4 are shown in Figure 2. For instructive  
196 purposes a point-like source having energies ( $E_0$ ) uniformly distributed between 0 and 8 MeV has been  
197 simulated. One can clearly notice that alpha particles show a probability of interacting with micromesh  
198 1. The latter plays an important role because its geometry allows only a certain range of incidence angle  
199 of alpha paths. The parameters of micromesh 1 are the diameter of the grid wire (18  $\mu\text{m}$ ), the distance  
200 between the axes of two adjacent wires (45  $\mu\text{m}$ ) and the material (stainless steel). The angle of incidence  
201  $\theta$  is the angle defined by the particle trajectory and the normal to the gas-sample interface. The cut-off  
202 angle  $\theta_{\text{max}}$  of the simulated micromesh has been estimated to 68°. The depth of the gas passed through  
203 (Z coordinate) as a function of the emission energy  $E_0$  of the alpha particle is displayed in Figure 3.

204 From the calculated 2D histogram (Figure 3, left), three types of alpha particle behaviour can be  
205 distinguished with respect to the detector.

206 - *Type-1: Alphas that do not pass through micromesh 1.* If  $E_0 < 40$  keV, the alpha range in  
207 the gas is less than the depth of the first amplification space (400  $\mu\text{m}$ ); this explains why  
208 particles with low emission energy never pass through micromesh 1. If  $E_0$  ranges from 40  
209 keV to 6 MeV, about 85% particles do not pass through micromesh 1. From 6 MeV onwards,  
210 this proportion decreases progressively to about 63% for  $E_0 = 8$  MeV. If  $E_0 > 40$  keV, an  
211 alpha particle deposits part of its energy in the first amplification space and may or may not  
212 be stopped by micromesh 1. For example, when an alpha particle is emitted with an angle  
213 of incidence  $\theta > \theta_{\text{max}}$ , then it is always stopped by micromesh 1. Note that the probability of  
214 an alpha particle passing through micromesh 1 increases slightly with  $E_0$ . Finally, it is  
215 deduced that it is difficult to exploit type-1 alphas for spectroscopic measurements, as the  
216 energy deposition in the gas is not sufficient due to the small depth of the first amplification  
217 space. The fact that these alphas represent on average 80% of the total count is a factor  
218 limiting the efficiency of the spectroscopic measurement.

219 - *Type-2: Calorimetric alphas.* These alphas pass through micromesh 1, but do not reach  
220 micromesh 2. The deposited energy of type-2 alphas is equal to the emission energy. For 40  
221 keV < E<sub>0</sub> < 1 MeV, the particles passing through micromesh 1 are totally calorimetrized in  
222 the gas, i.e., none of them ever reach micromesh 2. For 1 MeV < E<sub>0</sub> < 2.7 MeV, the  
223 proportion of calorimetrized alpha particles gradually decreases until it becomes zero. For  
224 E<sub>0</sub> > 2.7 MeV, the proportion of calorimetric alpha particles is generally low. This effect is  
225 due to the cut-off angle which imposes a maximum range in the gas (and consequently a  
226 maximum energy of 2.7 MeV for which a particle cannot be stopped in the gas after passing  
227 through micromesh 1). Nevertheless, this proportion tends to increase to about 10 % for E<sub>0</sub>  
228 = 8 MeV. This increase for high E<sub>0</sub> can be explained by the fact that at high energies, alpha  
229 particles that interact with micromesh 1 can continue their path to be calorimetrized. These  
230 events will be considered as "polluting events" for the proposed application. The type-2  
231 alphas represent on average only 5% of the alphas emitted by the simulated uniform source.  
232 The fact that these alphas were not used for the spectroscopy is explained below in more  
233 detail.

234 - *Type-3: through-going alpha.* These are the alpha particles that have managed to pass  
235 through the entire depth of the gas and end up in the anode of the detector (at the Z = 1 cm  
236 coordinate). The energy deposited is therefore different from the initial energy. They  
237 represent on average 15% of the events recorded. On the green curve, the proportion of the  
238 crossing particles is constant and around 20% from 2.7 MeV. Around 6 MeV, there is a  
239 theoretical increase in the proportion of the particles passing through with energy. These  
240 alphas will be highlighted below because they exhibit a link between E<sub>0</sub> and the deposited  
241 energy.

### 242 **2.2.2 From deposited energy to emission energy**

243 To exploit the energy deposited by the crossing particles, the length d of the alpha track will be used:-

$$244 \quad d = \sqrt{x^2 + y^2 + z^2} \text{ (cm)} \quad 1$$

245 where x and y are the projected distances along the X and Y axes respectively, and z the thickness of  
246 the gas passed through along the Z axis. However, z is an unknown for type-2 alphas because the detector  
247 does not allow us to measure this coordinate: it is not a time projection chamber. This explains why  
248 type-2 alphas are not used for spectroscopy. Nevertheless, for type-3 alphas, it is possible to fix z to the  
249 thickness of the detector (1 cm).

250 Knowing the deposited energy E<sub>dep</sub> and the length of the track d, it is possible to relate E<sub>dep</sub>/d to the  
251 emission energy of the alpha particle E<sub>0</sub>. For this, Monte Carlo simulation was used to determine the  
252 distribution E<sub>dep</sub>/d as a function of E<sub>0</sub> for all alpha particles types (Figure 4).

253 The three types of alpha events described above can be observed in Figure 4, being indicated by three  
254 zones of visible colour on the right-hand distribution. Firstly, the area bordered in green corresponds to  
255 the alphas that pass completely through the detector (type-3). For these alphas, the function  $E_{\text{dep}}/d =$   
256  $f(E_0)$  follows a bijection. The result is equivalent to the averaged Bethe curve. Secondly, the area  
257 bordered in red corresponds to the calorimetrized alphas (type-2). These alphas disrupt the expected  
258 bijective contribution between 1 MeV and 3 MeV. Thirdly, the alpha events in the orange-bordered area  
259 are those that do not pass through micromesh 1 (type-1). The length  $d$  is greatly overestimated which  
260 induces  $E_{\text{dep}}/d < 200$  keV/cm for most of these events. Only those alphas that contribute to the bijective  
261 distribution (type-3 alpha - selection in green) are selected; calorimetrized alphas (type-2) cannot be  
262 considered for the analysis because they fall outside the bijective zone. Moreover, the type-2 alpha has  
263 initial energy  $E_0$  directly proportional to  $E_{\text{dep}}$ . But type-2 alpha cannot be used for energy measurement  
264 above 2.7 MeV because their proportion is close to zero (except for “polluting events”). For application  
265 to the  $^{238}\text{U}$  series, the measurement range needs to be up to 8 MeV. The way of selecting type-3 alphas  
266 is detailed in the next section.

## 267 **2.3 Analysis method for spectral reconstruction**

268 According to the simulation, it has been shown that among the three types of events generated, only  
269 type-3 alphas can be used for reconstructing the energy spectrum (from 3 MeV to 8 MeV). The low  
270 threshold of 3 MeV will be further explained in section 2.3.4. Only the alphas passing through the  
271 detector can be used for a spectral reconstruction beyond 3 MeV, because in this case the length ( $d$ ) of  
272 the track is known and the deposited energy tends to avoid the Bragg peak at the end of the path. This  
273 section describes the method for measuring the energy ( $E_0$ ) spectrum of an alpha-emitting source using  
274 the charge histograms.

### 275 **2.3.1 Particle identification**

276 The question is now to find a criterion to select type-3 alphas only. The statistical criterion used is  
277 kurtosis, calculated on the charge histograms collected on the anode. The kurtosis coefficient can be  
278 interpreted as a “shape feature” for charge histograms: a high value of kurtosis indicates that the  
279 distribution is rather concentrated; in contrast, a low value of kurtosis describes a flat distribution.  
280 Normalized kurtosis was used for the calculation (see equation 3). It is -1.2 for a continuous uniform  
281 distribution, and rises to +3 for a Laplace distribution. It is 0 for a normal distribution. This coefficient  
282 is useful because in most of the cases, the traversing alpha (type-3) does not deposit the "Bragg peak"  
283 at the end of the path: it presents a flatter profile than the calorimetric alpha (type-2) ones. But in a few  
284 cases, the peaked characteristic of the Bragg curve can be present in charge histograms for type-3 alpha.  
285 Moreover, calorimetric alpha can have a charge distribution close to flat. Such a wide range of behaviour  
286 makes it difficult to show a perfect discrimination between type-2 and type-3 alpha. Figure 5 (on the  
287 left) gives an example of a charge histogram. The amplification "peak" is located here at position  $X = 0$

288 cm while the "Bragg peak" is located at  $X = -1.2$  cm. This is why it is necessary to ignore the  
289 amplification peak for the calculation of kurtosis.

290 If  $X$  is a real random variable defined on an interval, then the kurtosis of  $X$ ,  $Kurt(X)$ , is defined such  
291 as:-

$$Kurt[X] = E \left[ \left( \frac{X - \mu}{\sigma} \right)^4 \right] = \frac{\mu_4}{\sigma^4} \quad 2$$

292 and the normalised kurtosis is:-

$$KurtNorm[X] = Kurt[X] - 3 \quad 3$$

293

294 where  $E$  is the mathematical expectation;  $\mu = E(X)$ , the average of  $X$ ;  $\mu_4$  is the central moment of order  
295 4; and  $\sigma$ , the standard deviation. Kurtosis is calculated bin by bin on the charge histograms. Figure 6  
296 shows the kurtosis distribution for the three types of alpha particles. The kurtosis of the type-3 alphas  
297 shows a different distribution; for example, the majority of the type-3 alphas have a kurtosis close to -  
298 1.2 (green distribution, Figure 6) while type-1 and type-2 alphas exhibit a kurtosis above -1.

299 By selecting the peak related to the type-3 alphas, most of the alpha which are not usable for  
300 spectroscopic measurement is eliminated. The upper boundary of the peak selection is at the interface  
301 between the "pass-through" particles (green) and the calorimetrized particles (red). This interface is not  
302 clearly defined as an overlap occurs between the green and red curves. However, by placing the  
303 threshold at the intersection, on the abscissa there is a low percentage (3.4%) of calorimetrized particles  
304 selected (against 95.8 % of pass-through alpha selected, and 0.8 % of alpha that do not pass through  
305 micromesh 1). The setting of this threshold was optimized to reduce this percentage but without lowering  
306 the final efficiency. An identical kurtosis calculation was also performed on the  $Y$  charge histogram.  
307 Considering the charge histograms according to  $X$  and  $Y$  and using  $kurt(X) < -1.1$  &  $kurt(Y) < -1.1$ ,  
308 6.4% of the events were selected from all the detected alphas used for autoradiography analysis. Once  
309 the (-1.1) threshold is defined, it is a constant that does not depend on any gains which can be  
310 subsequently applied to the deposited energy.

### 311 **2.3.2 Measurement of the energy deposited in the gas by the alpha particles**

312 The energy deposited ( $E_{dep}$ ) by an alpha particle in the gas is the sum of the energy deposited in the drift  
313 space and the amplification space 1.  $E_{dep}$  is calculated considering both the charge deposits along the  $X$   
314 and  $Y$  axis. Figure 5 shows a simulated charge histogram along the  $X$  axis. This is the type of data  
315 provided by the PIM detector where the algorithm is applied.

316 The relationship between the deposited energy  $E_{dep}$  lost by an alpha particle to create the primary number  
317 of charges measured is given by the following equation:-

$$E_{dep} = W \times nb_{Primary\_charge} \quad 4$$

318 where  $W$  (eV) is the average ionisation energy (in neon gas  $W = 36$  eV). The energy can be determined  
 319 from the integral of the charge histogram (Figure 5, right). The energy deposited in the total gas volume  
 320 of the detector along the X axis ( $E_{depX}$ ) is not the integral of the entire charge histogram, but only the  
 321 integral of the green area (right of Figure 5).  $E_{depX}$  can be determined using the decomposition depicted  
 322 in Figure 5 (right), following equation 5:-

$$E_{depX} = E_{totalX} - E_{peakX} + E_{extrapolationX} \quad 5$$

323 where  $E_{totalX}$  is the integral of energy measured all along the track (in the drift space and amplification  
 324 space 1),  $E_{peakX}$  the integral of energy in the amplification peak ( $E_{peakX} = E_{1x} + E_{extrapolationX}$ ), and  
 325  $E_{extrapolationX}$  is the energy corresponding to the mean of the primary charges created in the amplification  
 326 space and multiplied by  $W$ . The same calculation is performed for determining  $E_{depY}$  for the charge  
 327 histogram relates to the Y axis,  $E_{dep}$  being finally obtained by  $E_{depX} + E_{depY}$ . The charges related to  $E_{dep}$   
 328 measurement undergo several stages of amplification and drift, which degrades the resolution on the  
 329 measured  $E_{dep}$ . The main charge peak cannot be used to determine  $E_0$  because it corresponds to the  
 330 energy deposited in the first amplification zone. This one undergoes a gain which is a function of the Z  
 331 position of the charge created in the amplification space. During this process, the information on the  
 332 deposited energy is thus degraded. As a consequence, the energy resolution would be insufficient using  
 333 the main charge peak because the energy deduced from the main peak would be difficult to compare to  
 334  $E_{dep}$ .

### 335 **2.3.3 Length of ionisation tracks of particles in the gas, and selection of long tracks**

336 As stipulated previously in section 2.2.2 the calculation of track length is only possible for particles  
 337 passing through the whole thickness of the detector. Nevertheless, an additional selection criterion of  
 338 the tracks is necessary. Indeed, some of the preserved tracks correspond to alphas transmitted with a low  
 339 angle of incidence. This implies that the deposited energy will be overlapped with the amplification  
 340 peak. Moreover, a certain number of bins is necessary for the calculation of  $E_{extrapolation}$ . Therefore, a  
 341 minimum projected track length  $d_{proj} = \sqrt{dx_{min}^2 + dy_{min}^2}$  is required in order to correctly  
 342 measure the deposited energy. This minimum length is set to  $d_{proj} = 0.71$  cm as  $dx_{min} = dy_{min} = 0.5$   
 343 cm. (this length corresponding to 5 bins of the charge distribution in  $E_{peak}$  plus 8 bins to calculate  
 344  $E_{extrapolation}$  and  $E_{dep}$ , where 1 bin is equal to  $400 \mu\text{m}$ ). By applying this distance filtering in the X and Y  
 345 axes, an overall theoretical efficiency of 5% is obtained for the spectral reconstruction. Note that this  
 346 filtering also allows the elimination of a very large number of particles that do not pass through  
 347 micromesh 1. Only 0.075% of these particles are selected by this distance filtering. Thus, the pollution  
 348 from these particles is considered as negligible. To summarize, extracting  $E_{dep}$  from the charge  
 349 histograms imposes a selection on  $d_{proj}$  in addition to the kurtosis criterion; these selections reduce the  
 350 theoretical efficiency to 5%. This efficiency is the amount of alpha selected for the energy spectrum  
 351 reconstruction divided by the amount of alpha reaching the detector and used to create the

352 autoradiograph image. By calculation, 37% of the whole type-3 alphas are selected for energy  
353 reconstruction.

#### 354 **2.3.4 Reconstruction of the energy spectrum of the source**

355 The energy  $dE$  lost by a particle per unit length  $dX$  in a medium is defined by the linear stopping power  
356  $S = -dE/dx$  (MeV/cm). This can be described for a charged particle by the Bethe formula [50]. The  
357 stopping power depends on both the kinetic energy of the particle, and the transverse medium. The  
358 stopping power (or the mass stopping power  $S.1/\rho$ ) is referenced on the ASTAR database [51] and  
359 plotted as a function of the kinetic energy for alpha particles in Supplementary Material, Figure S2. For  
360 the range of 2 MeV to 100 MeV the near-linearity of the log-log plot over  $S$  Energy suggests a power  
361 law relationship of the form  $dE/dx = cE^d$  or reciprocally  $E = a(dE/dx)^b$ . For a non-relativistic particle, at  
362 moderate energies, the Bethe formula is dominated by  $1/v^2$  or inversely with particle energy, suggesting  
363  $b = 1$ . However, it represents only a theoretical approximation; furthermore, the Bethe formula breaks  
364 down at very low energy. So, the power function with “b” and “a” as parameters will be used in this  
365 section as a fitting function to establish the relationship between  $E_{dep}/d$  and  $E_0$ .

366 In addition, a gaseous detector needs amplification in order to have enough charge collected to detect a  
367 signal above the electronic noise. So, the energy deposited in the gas ( $E_{dep}$ ) can be defined as an initial  
368 energy deposited in the gas ( $E_{dep\_ini}$ ) multiplied by a gain  $G_2$  created by the amplification space 2:-

$$E_{dep} = G_2 \times E_{dep\_ini} \quad 6$$

369 The emission energy  $E_0$  of the particle is calculated as a function of the energy deposited in the gas ( $E_{dep}$ )  
370 and the length of the track ( $d$ ) by applying a power function (equation 7), which corresponds to the fit  
371 of the bijection linking  $E_{dep}/d$  and  $E_0$  obtained on the type-3 alpha (see above Figure 4):-

$$E_0 \left( \frac{E_{dep}}{d} \right) = a \times \left( \frac{E_{dep}}{d} \right)^b \quad 7$$

372 For any gain  $G_2$ , the power law for the calibration function can be written as equation 8:-

$$E_0 \left( \frac{E_{dep}}{d} \right) = a \times \left( \frac{G_2 \cdot E_{dep\_int}}{d} \right)^b \quad 8$$

373 For a detector without gain (i.e.  $G_2 = 1$ ), there is a new function with new coefficient  $a'$  and  $b'$  defined  
374 in equation 9.

$$E_0' \left( \frac{E_{dep\_ini}}{d} \right) = a' \times \left( \frac{E_{dep\_int}}{d} \right)^{b'} \quad 9$$

375 There is an equality with energy measurement  $E_0 = E_0'$ , which means that (8) = (9). Theoretically,  $b$   
376 must depend only on the physical parameters of the detector, mainly the density and the gas composition.  
377 That results in the calculation of  $G_2$  in equation 10:

$$\begin{cases} b = b' \\ G_2 = \left(\frac{a'}{a}\right)^{\frac{1}{b}} \end{cases}$$

378 In order to simplify the simulation, the choice was made to fix  $G_2 = 1$ . In this case  $E_{\text{dep}}$  is equal to  $E_{\text{dep\_ini}}$   
 379 and the coefficients become  $b = b' = b_{\text{sim}}$ , and  $a = a' = a_{\text{sim}}$ .

380 Figure 7 illustrates the relationship between the energy deposited by the particles in the gas per unit  
 381 length ( $E_{\text{dep}}/d$ ) and the initial energy of the particles ( $E_0$ ) more precisely. The parameters  $a_{\text{sim}}$  and  
 382  $b_{\text{sim}}$  of this power law are determined by adjustment (see red curve Figure 7). The fit gives  $a_{\text{sim}} =$   
 383 20183600 and  $b_{\text{sim}} = -1.26$ .

384 This distribution has been drawn without plotting the alpha that interact with micromesh 1 and lose part  
 385 of their energy inside it. The effect of those alpha is visible on Figure 8 where  $E_{0\_reconstructed}$ , a  
 386 function of  $E_{0\_initial}$ , should follow a linear function if the spectral reconstruction succeeds. For 74.5 %  
 387 of alpha, it is the case. But for 24 % the initial energy is modified. This modification is not an error of  
 388 reconstruction because it is intrinsically due to interaction between the alpha and micromesh 1 (alpha  
 389 can be of type-2 or -3). However, the selected alpha with  $E_0 < 1.5$  MeV (1.5 %) do not follow the power  
 390 reconstruction function precisely. Those effects are visible in the final energy spectrum reconstruction  
 391 on Figure 9.

392 Figure 9 (left) gives the initial energy spectrum  $E_0$  obtained with the algorithm described in this section,  
 393 which would have been a uniform spectrum between 0 MeV and 8 MeV. The corresponding efficiency  
 394 Figure 9 (right) is the number of alpha selected in the spectrum with original energy  $E_0$ , divided by the  
 395 number of alpha generated by the source at  $E_0$  energy.

396 Firstly, on the reconstructed spectrum, an under-count of around 8 MeV is observed, caused by the effect  
 397 of energy resolution. Secondly, between 2 and 3 MeV, an over-count is observed, caused by: (1)  
 398 calorimetric particles which are not filtered by the kurtosis criterion (with  $E_0 < 1.5$  MeV) and which are  
 399 reconstructed as higher energy they have; and (2) alphas which lose energy because of micromesh 1.  
 400 Thirdly, another effect is visible on the reconstructed spectrum. It looks as if the spectrum decreases  
 401 slightly from 4 to 8 MeV which is contradictory to the efficiency curve. This does not stem from the  
 402 efficiency of the detection method. Such behaviour is inherited from the selected alpha which interact  
 403 and lose energy inside micromesh 1 and change the final distribution of reconstructed energy.

404 As a consequence, the range of the spectrum lower than 3 MeV has not been used because of the over-  
 405 count in that range. The maximum energy studied is 8 MeV (this is a limitation coming from  $^{238}\text{U}$  series).  
 406 The valid measurement ranges from 3 to 8 MeV. In this case, the mean efficiency is defined by the  
 407 number of alpha falling inside this energy range [3-8 MeV] divided by the total number of alpha  
 408 detected, and has a value of 3.9 %.

409 The Geant4 simulation used in this section has its own limitations. For instance, thermodynamics  
410 phenomena (variations of temperature and pressure) are not considered, as well as electronic noise  
411 associated to the ASIC reading. Moreover, electric fields, recombination phenomena and grid  
412 transparency are not considered. The electron drift speed is not taken into account in the proposed  
413 simulations ( $V_d_{\text{electron}} = 5 \text{ cm}/\mu\text{s}$ ), which may induce shifts in the charge measurement between the  
414 beginning and end of the track. No physical simulation of the gain  $G_2$  in the second amplification space  
415 (this gain is considered as unitary) has been performed. Some parameters of the simulation are defined  
416 after experimental feedback, such as the amplification gain in the first space. The proposed simulation  
417 is however sufficient to obtain data and spectra comparable to those measured by the PIM detector. By  
418 analysing these data, a methodology is established here that enables the measurement of an energy  
419 spectrum of an alpha particle source.

### 420 **3 Results**

421 The previous section described a method to theoretically measure an energy spectrum for alpha particles.  
422 In order to apply this method to real samples it is important to develop a calibration method. A calibrated  
423 sample with multiple radionuclides was used.

#### 424 **3.1 Thin source of $^{226}\text{Ra}$ used for calibration**

425 The calibration source described (named  $^{226}\text{Ra}$  source) is a disk (NucFilm Disc<sup>TM</sup>) composed of a thin  
426 layer of manganese dioxide containing radium-226. This source covers a polyamide support of 24 mm  
427 diameter. The  $^{226}\text{Ra}$  is trapped in a 20 mm diameter area. The  $^{226}\text{Ra}$  decays and emits an emission energy  
428 spectrum which is assimilated to that of a thin source including the  $^{226}\text{Ra}$  and its decay products  
429 (Supplementary Material, table S1).

430 In Figure 10 the spectrum of the  $^{226}\text{Ra}$  source was measured using an alpha spectrometer CANBERRA  
431 model 7401, coupled with a passivated implanted planar silicon (PIPS) detector for alpha spectroscopy  
432 (A450-18AM, 450 mm<sup>2</sup>, 18 keV FWHM at 5.486 MeV). The  $^{226}\text{Ra}$  activity is higher than for its  
433 daughters. For an acquisition time of 28811 s (~8h), the recorded counting rate is 0.28 cps for an energy  
434 spectrum ranging from 1 to 8 MeV. The alpha spectrum is not that of a perfectly fine source, but it  
435 comes close. For the presented application, this source is nevertheless considered as a fine source  
436 because the width of the observed peaks is well below the energy resolution of the used device.

437 The measurement was conducted using a large area sample holder (12 x 8 cm<sup>2</sup>) with the BeaQuant,  
438 using Alpha-mode, with the  $^{226}\text{Ra}$  source in the center of the sample holder. This sample holder was a  
439 little different from the configuration used in the simulation. In this case, the source needed to be placed  
440 on another micromesh. Each contact between this micromesh and the source reduced the number of  
441 alpha detected, and introduced an optical transparency of 51%. But this new component did not change  
442 the methodology used for the energy measurement. The autoradiograph representing the spatial  
443 distribution of the radioactivity on the source surface is shown in Figure 11.

444 To determine the a and b parameters of equation 7, it was necessary to use a calibration source during  
 445 each acquisition. This source had to contain two sufficiently distinct energy peaks  $E_{cal1}$  and  $E_{cal2}$ ,  
 446 separated by at least 2 MeV, in a range between 3.5 and 8 MeV; the  $^{226}\text{Ra}$  source with its daughters was  
 447 then used as a calibration source. Its emission spectrum contains the main  $^{226}\text{Ra}$  peak at 4784 keV and  
 448 the  $^{214}\text{Po}$  peak at 7686 keV. In this sample, the system of two equations with two unknowns to be solved  
 449 is the following (equation 11):-

$$\begin{cases} a \times x_1^b = E_{cal1} \\ a \times x_2^b = E_{cal2} \end{cases} \quad 11$$

450 where  $x_1$  and  $x_2$  are the values of  $E_{dep}/d$  associated respectively with  $E_{cal1} = 4670$  keV and  $E_{cal2} = 7392$   
 451 keV. These values are calculated by fitting the degraded alpha energy spectrum of Figure 10, to take the  
 452 detector energy resolution into account. This degraded alpha energy spectrum is obtained by convolving  
 453 the spectrum on Figure 10 by a normal law of fixed standard deviation ( $\sigma = 342$  keV). Because the  
 454 energy resolution is “worth” more than the energy resolution of the spectrum on Figure 10, the two  
 455 energy peaks  $E_{cal1}$  and  $E_{cal2}$  do not correspond to the peaks defined above. An average of energy around  
 456 the two peaks results from this degradation, which is however very close to their theoretical values.  
 457 Moreover, the corresponding theoretical energy is also shifted by the sample thickness.

458 The expression of a and b is deduced by equation 12:-

$$\begin{cases} b = \frac{\ln\left(\frac{E_{cal1}}{E_{cal2}}\right)}{\ln\left(\frac{x_1}{x_2}\right)} \\ a = \sqrt{E_{cal1} * E_{cal2}} * e^{-b \ln(\sqrt{x_1 x_2})} \end{cases} \quad 12$$

459 To determine the variables  $X_1$  and  $X_2$ , a fitting of the  $E_{dep}/d$  distribution (Figure 12) is performed using  
 460 two Gaussian functions. These histograms were built after selecting particles passing through the  
 461 detector according to the method described in Section 2.3. The values of  $X_1$  and  $X_2$  correspond to the  
 462 expectation of each normal distribution. In the example of the  $^{226}\text{Ra}$  source studied,  $X_1 = 22220$   
 463 channels/cm and  $X_2 = 15686$  channels/cm.

464 The calibrated values of the coefficients calculated using equation 12 are  $b = -1.31$  and  $a = 2422661904$ .  
 465 It can be seen that a and b are different from the simulation ( $a_{sim}$  and  $b_{sim}$ ), and this shows the need  
 466 for a calibration.

467 Finally, the energy  $E_0$  is measured particle by particle with the power law defined with the parameters a  
 468 and b calculated previously. Figure 13 shows the spectrum reconstructed with this power law. The  
 469 spectrum is plotted on Figure 13 (in red) and superimposed on the alpha spectrum obtained with alpha  
 470 spectrometry after degradation. It is consistent with the spectrum of the source measured by alpha  
 471 spectrometry and confirmed the hypothesis that the proportion of  $^{226}\text{Ra}$  has remained constant over time.  
 472 The energy resolution of the PIM detector can also be deduced from these results. It is measured at 7.3

473 % (K = 1) or 17.2% FWHM at 4647 keV by fitting the corresponding peak with a normal distribution.  
 474 The corresponding reconstruction efficiency is 5.4 % between 3 and 8 MeV.  
 475 The coefficient “a” depends on the gain  $G_2$  corresponding to the second amplification space. This gain  
 476  $G_2$  is a constant multiplication factor applied to  $E_{dep}$  for all alpha events and can vary from one  
 477 acquisition to another. The method to determinate the coefficient “a” (or indirectly  $G_2$ ) is described in  
 478 the next section.

479

### 480 **3.2 Calibration optimisation when the gain $G_2$ is variable**

481 It can be seen that the “a” coefficient from the calibration method is far higher than from the simulation  
 482 “a\_sim”. Such a result is in agreement with the expression of the “a” coefficient, including the gain  $G_2$ .  
 483 Equation 13 gives the relation linking  $G_2$  and “a” coefficient:-

$$\begin{cases} b = b' \\ a = \frac{a'}{G_2^b} \end{cases} \quad 13$$

484 where a' and b' are coefficients from a real acquisition using gain  $G_2 = 1$ , and a and b are coefficients  
 485 from a real acquisition with any gain  $G_2$  (because  $b < 0$  and  $G_2 > 0$  then  $a > a'$ ).

486 It can be seen that  $G_2$  is easier to introduce because it gives a physical sense to the “a” coefficient.  $G_2$   
 487 can be determined thanks to the calibration process described hereafter.

488 Concurrently, the coefficients a' and b' cannot be determined experimentally because if we set  $G_2 = 1$   
 489 with the electronics, there will not be enough charge collected by the detector to go above the threshold  
 490 charge detection. However, the modelling described in Section 2.3 was achieved with  $G_2 = 1$  ( $E_{dep} =$   
 491  $E_{dep\_int}$ ). So, it is possible to fix the coefficient by  $a' = a\_sim$ . Another issue is that  $b' = b \neq b\_sim$ . So, if  
 492  $a\_sim$  is used, the results of  $G_2$  will not be the realistic value of the gain, but a relative value (because  
 493  $a\_sim$  is an approximation of a'):-

$$G_2 = \left( \frac{a\_sim}{a} \right)^{\frac{1}{b}} \quad 14$$

494 According to this method the value of  $G_2$  can be estimated with equation 14. With the calibration source  
 495 a calculated value is  $G_{2\_cal} = 38.16$ .

496 Now, the calibration processes can be optimized in order to calibrate “any” sample by calculating the  
 497 “a” coefficient. For that, the coefficient  $b = -1.31$  is fixed by the calibration method thanks to the  $^{226}\text{Ra}$   
 498 source. Then, the coefficient  $a' = a\_sim = 20183600$  is also fixed. Finally,  $G_2$  is calculated when the  
 499 difference  $\epsilon$  (defined in equation 15) between the spectroscopy chain alpha spectrum distribution after  
 500 degradation ( $S1_i$ ) and the spectrum distribution ( $S2_i$ ) is a minimum.  $G_2$  can be “adjusted” (so “a” also  
 501 changes).  $\epsilon$  is plotted in Figure 14 for different value of  $G_2$ .

$$\varepsilon(G_2) = \sqrt{\sum_{i=1}^n (S1_i - S2_i(G_2))^2}$$

502 By applying this minimization of error technique, a corresponding  $G_2 = 38.15$  was determined when  $\varepsilon$   
 503 is at its minimum.  $G_2$  is nearly identical to  $G_{2,cal}$  with the first calibration process. With this technique,  
 504 any sample can be calibrated if the alpha spectrum determined by alpha spectrometry is known.

### 505 **3.3 Application using a geological sample**

506 In order to test and validate the energy spectrum reconstruction method, an acquisition of a thick  
 507 geological sample exhibiting  $^{238}\text{U}$  and its decay products at secular equilibrium was achieved. The  
 508 results are described hereafter.

509 The source is a uranium ore from Congo (rock age 600 My), containing uraninite ( $\text{UO}_2$ ), and showing  
 510 some localized uranotile and coffinite alterations. It was prepared at Bessines sur Gartempe (France)  
 511 and comes from the historical collection of Orano Mining (sample 9689-03). The sample is in the form  
 512 of a 7 mm-thick uraninite "piece" placed in a resin and polished on its surface. The emission energy  
 513 spectrum of this source was measured with an alpha spectrometer CANBERRA model 7401 (Figure  
 514 15), over an acquisition time of 9671 s ( $\sim 2.5$  h). The measured counting rate is 83.7 cps between 3000  
 515 keV and 8000 keV.

516 The sample is considered as a multi-alpha thick source. The measured spectrum corresponds to the  
 517 superposition of eight energy steps coming from the eight alpha emitters of the  $^{238}\text{U}$  natural decay chain  
 518 (Supplementary Material, table S2). The source is at secular equilibrium, so that all isotopes from the  
 519 decay chain demonstrate the same alpha activity. In the  $^{238}\text{U}$  series, 2.5 My are approximately necessary  
 520 to reach secular equilibrium (corresponding to about ten periods of  $^{234}\text{U}$ ).

521 The autoradiograph image shown in Figure 16 (right) was performed with the large area sample holder  
 522 in order to be under the same conditions as the calibration source presented above in Alpha-mode. The  
 523 surface activity measured is 418 cps (or 0.9 cps/mm<sup>2</sup>). The acquisition time used for measuring a  
 524 spectrum on the whole section is 7239 s.

525 The spectrum of the  $^{238}\text{U}$  sample is measured by applying the spectral reconstruction method. This  
 526 spectrum is shown in red in Figure 17, and it was adjusted using the calibration method described in  
 527 section 3.2, with the error  $\varepsilon$  minimization. During this calibration, the spectrum taken as a reference for  
 528 the calculation of error is the one from Figure 15 which has been degraded by normal function  
 529 convolution (shown in blue on Figure 17). The calibration leads to the calculation of gain  $G_2 = 36.90$ .  
 530 The spectrum matches the alpha spectroscopy chain. The counting rate recorded in the range of [3-9]  
 531 MeV is 18.7 cps. So, the efficiency of the spectrum reconstruction is 4.4 % in this energy range, and the  
 532 PIM detector has 22.3 % of the efficiency of the alpha spectrometer described above. The superposition

533 region around 3 MeV is still visible. A slight decrease in efficiency at 4.5 MeV is also observed. Overall,  
534 the two spectra in Figure 17 are very similar.

535 The results mean that the PIM detector can both measure the position of alpha particles and measure  
536 their energy. The efficiency of the developed spectroscopic technique is globally low. This can be a  
537 detection limit for some applications if the sample activity is low. The acquisition time can also be  
538 adjusted to compensate with this low efficiency. For example, considering that 2000 entries in the energy  
539 spectrum are sufficient for interpretation, this corresponds to a count rate of 0.075 cps for one week of  
540 acquisition time. In terms of uranium content, and considering a 1 mm<sup>2</sup> region of interest, this count rate  
541 is related to about 3 wt% of uranium in secular equilibrium. If the application of the spectral modality  
542 seems feasible for multi-source, it needs to be tested more deeply for heterogeneous geological samples.

#### 543 **4 Conclusion**

544 The described energy spectrum measurement method is based on an algorithm applied to data of an ideal  
545 point source representing the interaction of alpha particles with a PIM detector, whose elements were  
546 geometrically optimized. The spectral reconstruction efficiency is 4.4%, and the energy resolution is  
547 poor compared to a semiconductor (but is still better than other technologies). In addition, the efficiency  
548 can surely be improved by using a sample holder in exactly the same configuration as shown in Figure  
549 1, and also by optimising the algorithm of energy reconstruction. However, these results already make  
550 it viable to use spectroscopic autoradiography on geological samples. This measurement will allow the  
551 study of the spatial distribution of uranium and its descendants in geo-materials by coupling SEM  
552 characterizations. For this purpose, a complementary complex radioactive source material modelling  
553 could be considered. The direct application of this dual modality (energy-position) of analysis will be  
554 the subject of future developments. The measurement of the radioactive equilibrium state of  
555 heterogeneous geological structures, and the quantitative mapping of <sup>226</sup>Ra radioactivity are now being  
556 actively studied.

#### 557 **Supplementary material**

#### 558 **Acknowledgements**

559 This work has been done within the framework of a CIFRE Ph. D thesis (n°2020/0166) convention  
560 between the University of Poitiers, ERM (SARL) (Poitiers, France) and ANRT. We would like to thank  
561 Marc Brouand (ORANO Mining company) for the samples preparation. We would like to thank Julie  
562 Champion from Subatech Laboratory for her valuable assistance during the spectroscopy measuring  
563 campaign.

#### 564 **References**

565 [1] F. Bourrel, P. Courrière, Radionucléides - Application : biologie moléculaire, Techniques de  
566 l'Ingénieur, V1 (2003) 3362 - 3363.

- 567 [2] P. Fichet et al., Tritium analysis in building dismantling process using digital autoradiography,  
568 Journal of Radioanalytical and Nuclear Chemistry, 291 (2012) 869 - 875.
- 569 [3] G.A. Boyd, Autoradiography in Biology and Medicine, Academic Press, 1955.
- 570 [4] A. Biegon, C. Mathis, W. Jagust, Autoradiography as a Tool for PET/SPECT Tracer Selection  
571 and Assessment, Academic Press, (1996) 26 - 33.
- 572 [5] O. Alitalo et al., Digital autoradiography for efficient functional imaging without anesthesia in  
573 experimental animals: Reversing phencyclidine-induced functional alterations using clozapine,  
574 Progress in Neuro-Psychopharmacology & Biological Psychiatry, 100 (2020) 109887.
- 575 [6] E. Muuri et al., Electronic autoradiography of  $^{133}\text{Ba}$  particle emissions; diffusion profiles in  
576 granitic rocks, Applied Radiation and Isotopes, 149 (2019) 108 - 113.
- 577 [7] N. Macé, P. Fichet et al., Use of quantitative digital autoradiography technique to investigate  
578 the chlorine-36-labelled radiotracer transport in concrete, Applied Geochemistry, 100 (2019)  
579 326 - 334.
- 580 [8] M. Voutilainen et al., Characterization of spatial porosity and mineral distribution of crystalline  
581 rock using X-ray micro computed tomography, C-14-PMMA autoradiography and scanning  
582 electron microscopy, Applied Geochemistry, 101 (2019) 50 - 61.
- 583 [9] G. Devès et al., Chemical element imaging for speleothem geochemistry: Application to a  
584 uranium-bearing corallite with aragonite diagenesis to opal (Eastern Siberia, Russia), Chemical  
585 Geology, 294–295 (2012) 190 - 202.
- 586 [10] S.M. Zhmodik et al., The study of distribution and forms of uranium occurrences in Lake Baikal  
587 sediments by the SSNTD method, Radiation Measurements, 40 (2005) 532 - 538.
- 588 [11] A.A. Ochmann, A.T. Solecki, CR-39 autoradiographic micromapping of rock sections of  
589 various alpha emitters content – calibration approach, Journal of Environmental Radioactivity,  
590 79 (2005) 127 - 136.
- 591 [12] T. Pi et al., Autoradiography of geological fluorite samples for determination of uranium and  
592 thorium distribution using nuclear track methodology, Sociedad Mexicana de Física, 53 (2007)  
593 57 - 60.
- 594 [13] S. Kodaira et al., Evidence of Local Concentration of  $\alpha$ -Particles from  $^{211}\text{At}$ -Labeled Antibodies  
595 in Liver Metastasis Tissue, Journal of Nuclear Medicine, 60 (2019) 497 - 501.
- 596 [14] J.M. Cole et al., Phosphor imaging as a tool for in situ mapping of ppm levels of uranium and  
597 thorium in rocks and minerals, Chemical Geology, 193 (2013) 127 - 136.
- 598 [15] T. Bäck, L. Jacobsson, The  $\alpha$ -Camera: A Quantitative Digital Autoradiography Technique  
599 Using a Charge-Coupled Device for Ex Vivo High-Resolution Bioimaging of  $\alpha$ -Particles,  
600 Journal of Nuclear Medicine, 51 (2010) 1616 - 1623.
- 601 [16] N. Chouin et al., Ex Vivo Activity Quantification in Micrometastases at the Cellular Scale Using  
602 the  $\alpha$ -Camera Technique, Journal of Nuclear Medicine, 54 (2013) 1347 - 1353.

- 603 [17] R. AL Darwish et al., Autoradiography Imaging in Targeted Alpha Therapy with Timepix  
604 Detector, Computational and Mathematical Methods in Medicine, (2015) e612580.
- 605 [18] C. Teyssier et al., Exploitation of the charge sharing effect in Timepix device to achieve sub-  
606 pixel resolution in imaging applications with alpha particles, Astroparticle, Particle, Space  
607 Physics and Detectors for Physics Applications, 7 (2012) 681 - 687.
- 608 [19] N. Benabdallah et al., Radium-223 Treated Primary Patient Bone Biopsy Analysis: Macro to  
609 Microscale Analyses and Dosimetry, Journal of Nuclear Medicine, 61 (2020) 531.
- 610 [20] N. Benabdallah, Optimisation de la dosimétrie en alphathérapie par approche multi-échelle :  
611 application au traitement des métastases osseuses par le  $^{223}\text{Ra}$ , PhD manuscript, Université  
612 Paris-Saclay, (2017).
- 613 [21] B.W. Miller, Radiation Imagers for Quantitative, Single-particle Digital Autoradiography of  
614 Alpha- and Beta-particle Emitters, Seminars in Nuclear Medicine, 48 (2018) 367 - 376.
- 615 [22] B.W. Miller et al., Quantitative single-particle digital autoradiography with  $\alpha$ -particle emitters  
616 for targeted radionuclide therapy using the iQID camera, Medical Physics, 42 (2015) 4094 -  
617 4105.
- 618 [23] L. Han, B.W. Miller, et al., Applications of iQID cameras, Proceedings SPIE Volume 10393,  
619 Radiation Detectors in Medicine, Industry, and National Security XVIII, (2017) 165 - 170.
- 620 [24] P. Sardini et al., Quantitative autoradiography of alpha particle emission in geo-materials using  
621 the Beaver™ system, Nuclear Instruments and Methods in Physics Research Section A:  
622 Accelerators, Spectrometers, Detectors and Associated Equipment, 833 (2016) 15 - 22.
- 623 [25] J. Donnard et al., Advancements of labelled radio-pharmaceutics imaging with the PIM-MPGD,  
624 Journal of Instrumentation, 4 (2009) P11022.
- 625 [26] J. Donnard et al., The micro-pattern gas detector PIM: A multi-modality solution for novel  
626 investigations in functional imaging, Nuclear Instruments and Methods in Physics Research  
627 Section A: Accelerators, Spectrometers, Detectors and Associated Equipment, 610 (2009) 158  
628 - 160.
- 629 [27] J. Donnard et al., High Spatial Resolution in  $\beta$ -Imaging with a PIM Device, IEEE Transactions  
630 on Nuclear Science, 56 (2009) 197 - 200.
- 631 [28] S. Billon, P. Sardini et al., From  $\text{Bq cm}^{-3}$  to  $\text{Bq cm}^{-2}$  (and conversely) – Part 1: a useful  
632 conversion for autoradiography. Journal of Radioanalytical and Nuclear Chemistry, 320 (2019)  
633 643 - 654.
- 634 [29] S.M.H. Pooya et al., Passive  $\alpha$ -particles spectrometry by polycarbonate SSNTD using new  
635 etching conditions, Radiation Physics and Chemistry, 77 (2008) 949 - 953.
- 636 [30] M.F. Zaki, Y.H El-Shaer, Particularization of alpha contamination using CR-39 track detectors,  
637 PRAMANA journal physic, 69 (2007) 567 - 574.
- 638 [31] O.A. Bondarenko et al., performance of alpha particle spectroscopy using a TASTRAK™  
639 detector, Radiation Measurements, 26 (1996) 59 - 64.

- 640 [32] Y. Morishita et al., Detection of alpha particle emitters originating from nuclear fuel inside  
641 reactor building of Fukushima Daiichi Nuclear Power Plant, *Scientific Reports*, 9 (2019) 581.
- 642 [33] Y. Morishita, Development of an alpha- and beta-imaging detector using a thin-stilbene plate  
643 for radon-222 progeny measurements, *Radiation Measurements*, 140 (2021) 106511.
- 644 [34] M. Janik et al., Optimization of the Timepix chip to measurement of radon, thoron and their  
645 progenies, *Applied Radiation and Isotopes*, 107 (2016) 220 - 224.
- 646 [35] M. Holik et al., Alpha calibration of the Timepix pixel detector exploiting energy information  
647 gained from a common electrode signal, *Journal of Instrumentation*, 14 (2019) C06022.
- 648 [36] C. Granja et al., Resolving power of pixel detector Timepix for wide-range electron, proton and  
649 ion detection, *Nuclear Instruments and Methods in Physics Research Section A: Accelerators,  
650 Spectrometers, Detectors and Associated Equipment*, 908 (2018) 60 - 71.
- 651 [37] J. Vallergera et al., High-resolution UV, alpha and neutron imaging with the Timepix CMOS  
652 readout, *Nuclear Instruments and Methods in Physics Research Section A: Accelerators,  
653 Spectrometers, Detectors and Associated Equipment*, 591 (2018) 151 - 154.
- 654 [38] B.W. Miller et al., The iQID camera: An ionizing-radiation quantum imaging detector, *Nuclear  
655 Instruments and Methods in Physics Research Section A: Accelerators, Spectrometers,  
656 Detectors and Associated Equipment*, 767 (2014) 146 - 152.
- 657 [39] Y. Morishita et al., Performance comparison of scintillators for alpha particle detectors, *Nuclear  
658 Instruments and Methods in Physics Research Section A: Accelerators, Spectrometers,  
659 Detectors and Associated Equipment*, 764 (2014) 383 - 386.
- 660 [40] J.J.M. Kouwenberg et al., Alpha radiation dosimetry using Fluorescent Nuclear Track Detectors  
661 *Radiation Measurements*, 113 (2018) 25 - 32.
- 662 [41] J.A. Bartz et al., An imaging spectrometer based on high resolution microscopy of fluorescent  
663 aluminum oxide crystal detectors, *Radiation Measurements*, 56 (2013) 273 - 276.
- 664 [42] N. Hasebe et al.,  $\alpha$ -particle spectrometer based on xenon gas ionization chamber using coplanar  
665 electrodes, *Nuclear Inst. and Methods in Physics Research Section A: Accelerators,  
666 Spectrometers, Detectors and Associated Equipment*, 925 (2019) 123 - 127.
- 667 [43] K. Iwasaki et al., Development of Gas Ionization Chambers with Coplanar Electrodes for Alpha-  
668 ray Spectrometry, *Proceedings of International Symposium on Radiation Detectors and Their  
669 Uses, JPS Conf. Proc*, 11, 010003 (2016).
- 670 [44] H. Ito et al., Development of an alpha-particle imaging detector based on a low radioactivity  
671 micro-time-projection chamber, *Nuclear Instruments and Methods in Physics Research Section  
672 A: Accelerators, Spectrometers, Detectors and Associated Equipment*, 953 (2020) 163050.
- 673 [45] Y. Morishita et al., Flexible alpha camera for detecting plutonium contamination, *Radiation  
674 Measurements*, 103 (2017) 33 - 38.

- 675 [46] A. Angileri et al., Mapping  $^{238}\text{U}$  decay chain equilibrium state in thin sections of geo-materials  
676 by digital autoradiography and microprobe analysis, *Applied Radiation and Isotopes*, 140  
677 (2018) 228 - 237.
- 678 [47] S. Billon et al., Quantitative imaging of  $^{226}\text{Ra}$  ultratrace distribution using digital  
679 autoradiography: Case of doped celestines, *Journal of Environmental Radioactivity*, 217 (2020)  
680 106211.
- 681 [48] J-F. Moyen et al., Multi-scale spatial distribution of K, Th and U in an Archaean potassic  
682 granite: a case study from the Heerenveen batholith, Barberton Granite-Greenstone Terrain,  
683 South Africa, *South African Journal of Geology*, 124, (2021) 53 - 86.
- 684 [49] T. Siiskonen, R. Pöllänen, Advanced simulation code for alpha spectrometry, *Nuclear*  
685 *Instruments and Methods in Physics Research Section A*, 550 (2005) 425 - 434.
- 686 [50] G.F. Knoll, *Radiation Detection and Measurement*, 3<sup>rd</sup> ed., John Wiley & Sons, New York,  
687 2000, p 31.
- 688 [51] ASTAR, available at <https://physics.nist.gov/PhysRefData/Star/Text/ASTAR.html>, (accessed  
689 on January 1st, 2022).

Figure 1: Principle of the PIM detector. An alpha particle is coming from the sample, and interacts with the gas within the chamber of the detector.

Figure 2: Alpha track visualization with Geant4 in the (X, Z) plane close to micromesh 1. The alpha source is a point source. Micromesh 1 is simulated by a set of bars parallel to the X and Y axes, the bars parallel to the Y axis in the (X, Y) plane are visible. The z distance between the source and micromesh 1 is 400  $\mu\text{m}$ .

Figure 3: Left: 2D histogram showing the depth of gas passed (Z in cm) as function of the alpha emission energy  $E_0$ . Right: Proportion of the three identifiable alpha event types as a function of  $E_0$ .

Figure 4: Bethe curves ( $E_{\text{dep}}/d = f(E_0)$ ) obtained using Geant4 simulations, for all types of alphas. Left: using  $d = \sqrt{x^2 + y^2 + z^2}$ , which cannot be experimentally measured; Right: using  $d = \sqrt{x^2 + y^2 + 1}$  which can be estimated using the PIM. The orange, red and green selections correspond to alpha types 1, 2 and 3, respectively.

Figure 5: Left: Boundaries used in charge histogram (in X here) for the calculation of kurtosis (for type-2 alpha event example). Right: schematic illustration of the total energy calculation.

Figure 6: Kurtosis distribution for the three alpha types; type-1 in blue; type-2 in red; type-3 in green.

Figure 7: Distribution of  $E_0$  according to  $E_{\text{dep}}/d$ , obtained for particles sorted by kurtosis and projected distance criteria (Bethe curve). The distribution is adjusted by a power law (in red).

Figure 8: Distribution of  $E_0$  reconstructed versus  $E_0$  initial when the particle leaves the source.

Figure 9: Left: Reconstructed spectrum, obtained from a uniform activity source; Right: efficiency of the reconstruction method.

Figure 10: Energy spectrum of the  $^{226}\text{Ra}$  source obtained with an alpha spectrometry chain (acquisition made in 2017).

Figure 11: alpha autoradiograph of the  $^{226}\text{Ra}$  source obtained with the autoradiograph. A surface counting rate of 0.32 cps was measured.

Figure 12: Distribution of  $E_{\text{dep}}/d$  for selected alpha particles of  $^{226}\text{Ra}$  calibration sample.

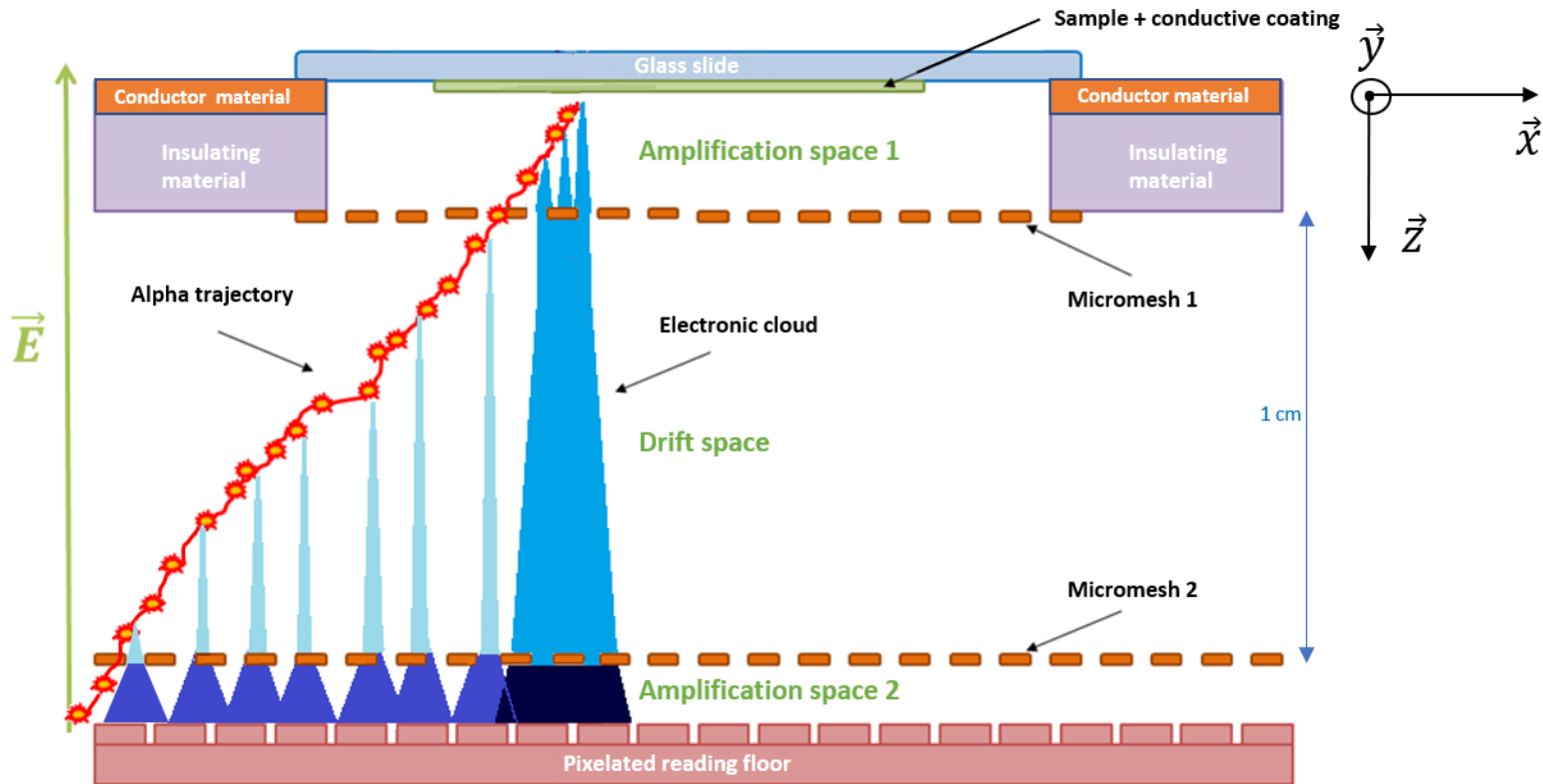
Figure 13: Comparison of the spectrum (divided by their respective internals) of the calibration source ( $^{226}\text{Ra}$ ) obtained experimentally with the PIM detector and SA method (red) with the spectrum obtained from the spectroscopy chain, after degradation (blue).

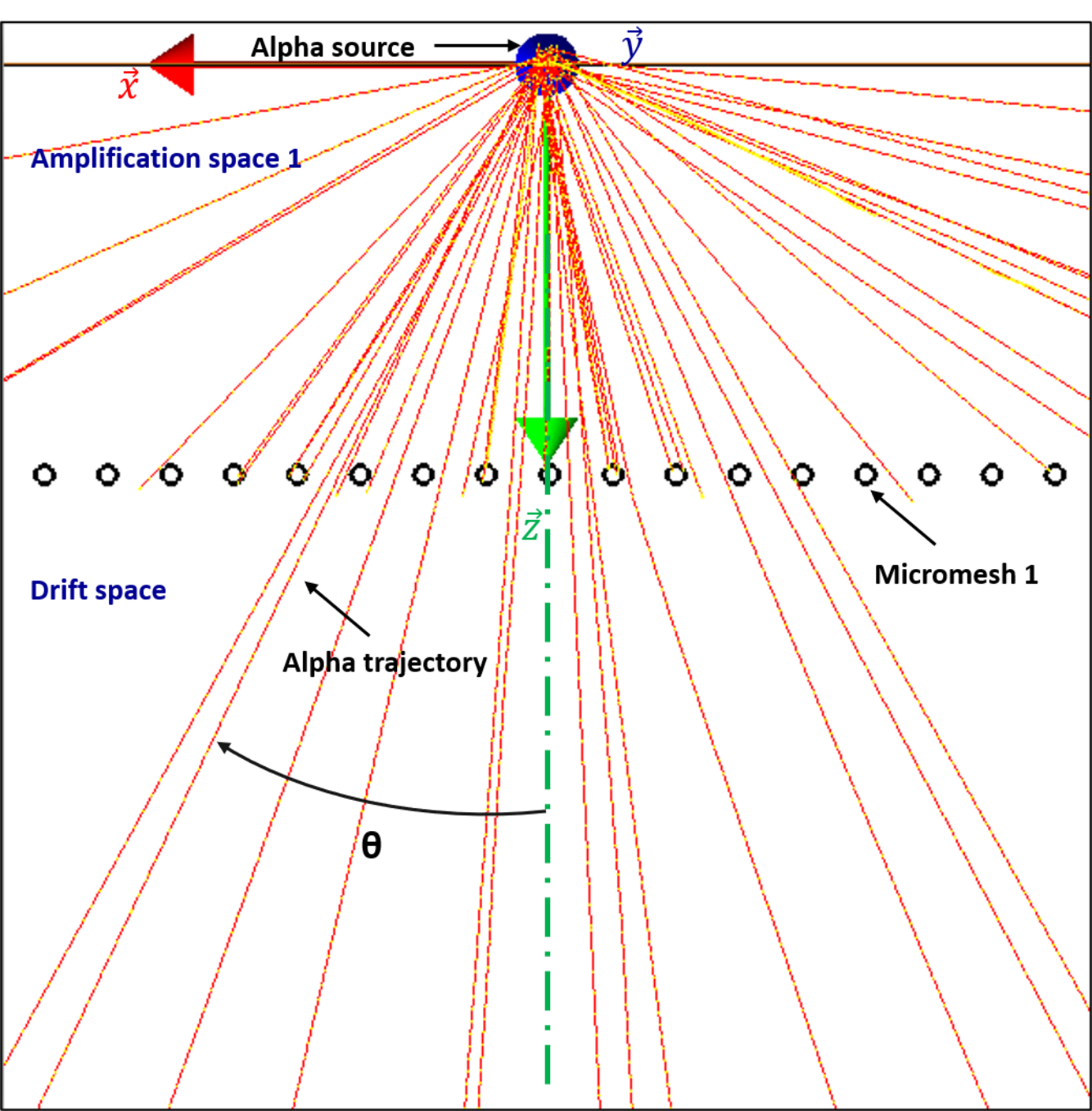
Figure 14: Difference between spectrum 1 (spectroscopy chain alpha spectrum distribution after degradation) and spectrum 2 (PIM detector spectrum depending of  $G_2$ ) distributions for  $^{226}\text{Ra}$  source, function of gain  $G_2$ .

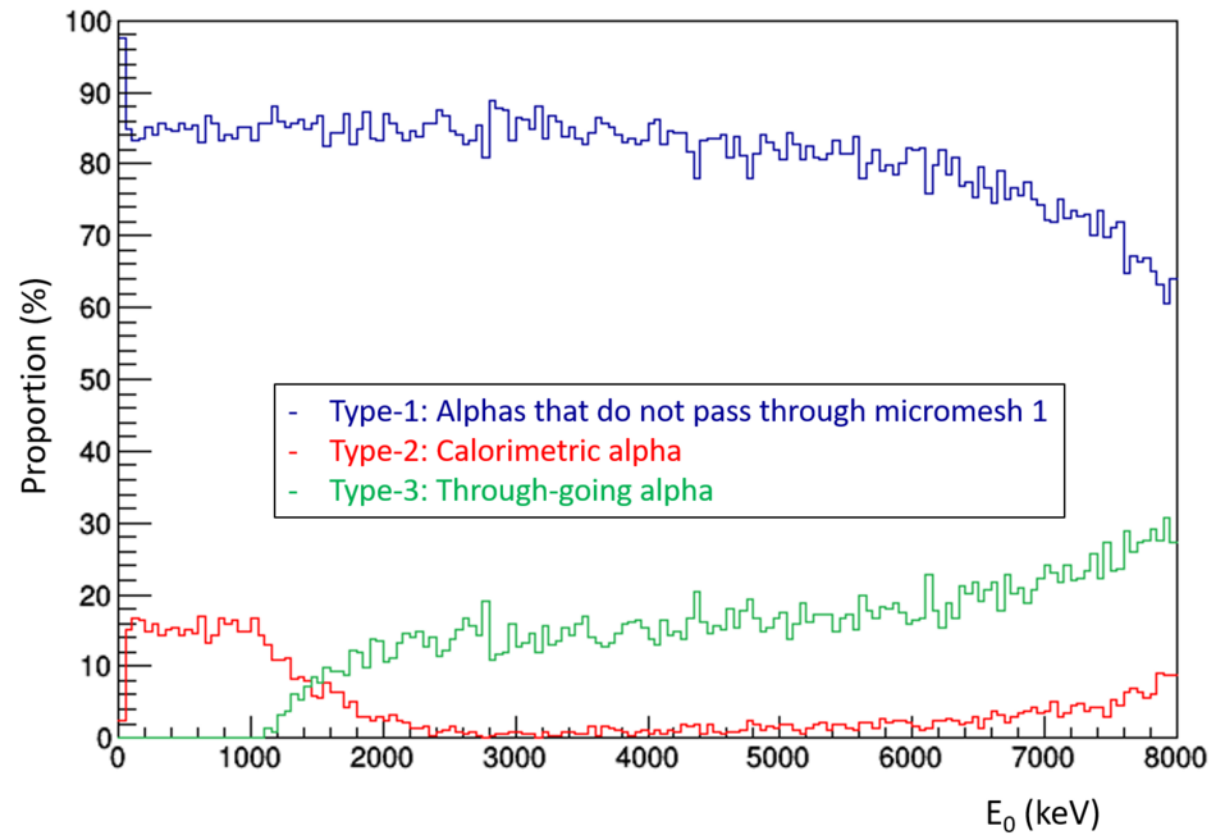
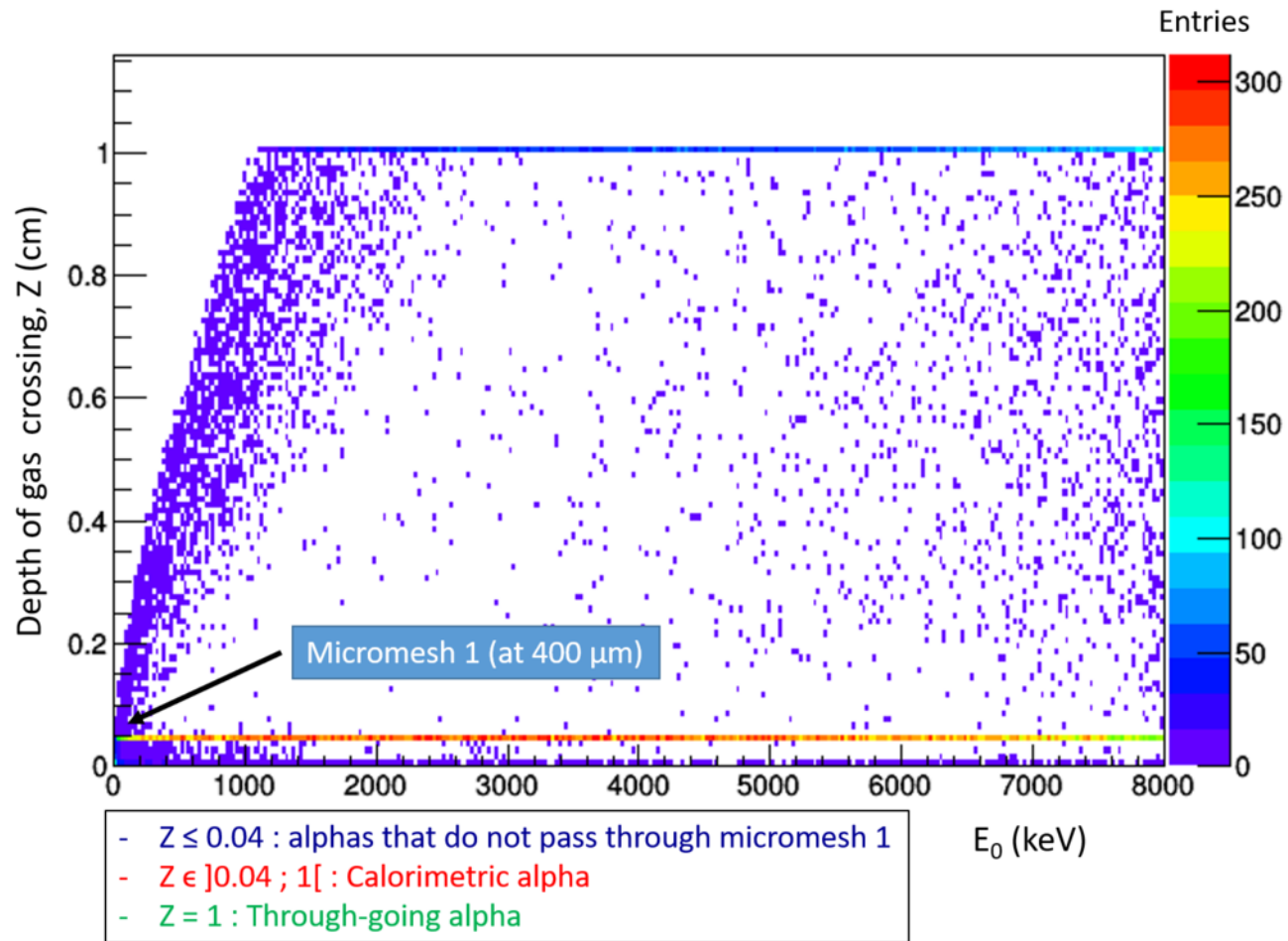
Figure 15: Energy spectrum of uranium ore sample measured by alpha spectrometry. There are 8 alpha emitters from the  $^{238}\text{U}$  decay product:  $^{238}\text{U}$ ,  $^{234}\text{U}$ ,  $^{230}\text{Th}$ ,  $^{226}\text{Ra}$ ,  $^{222}\text{Rn}$ ,  $^{218}\text{Po}$ ,  $^{214}\text{Po}$  and  $^{210}\text{Po}$ .

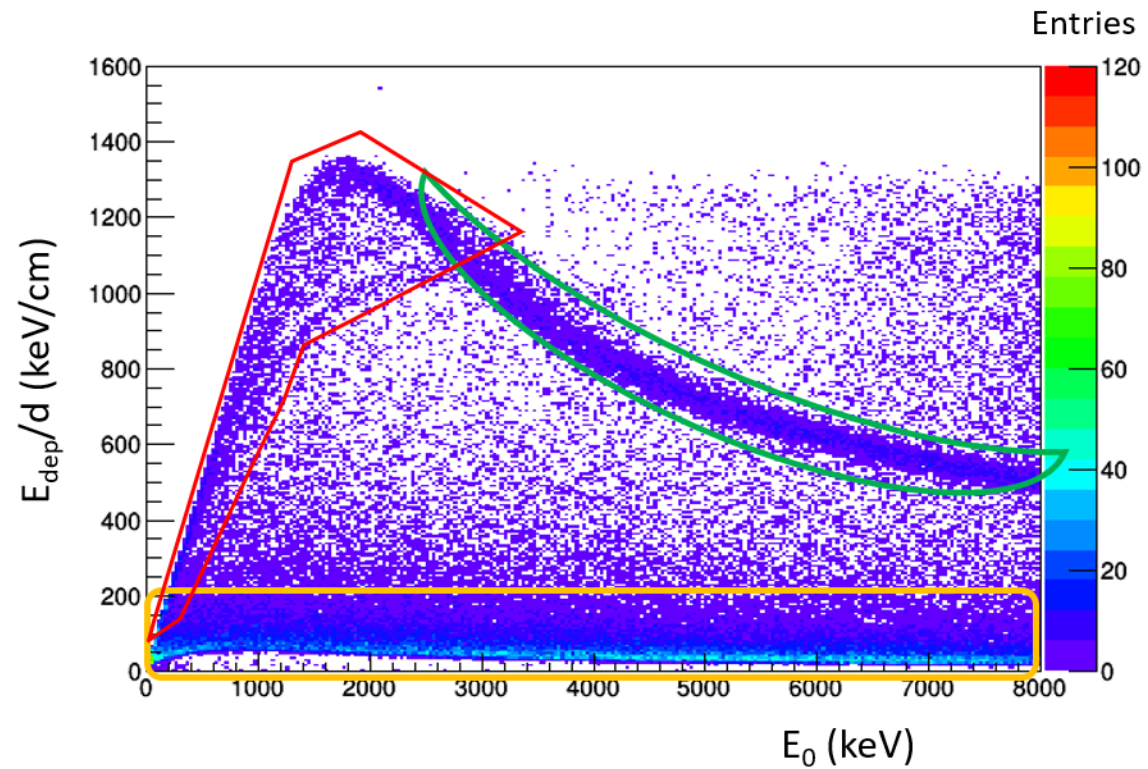
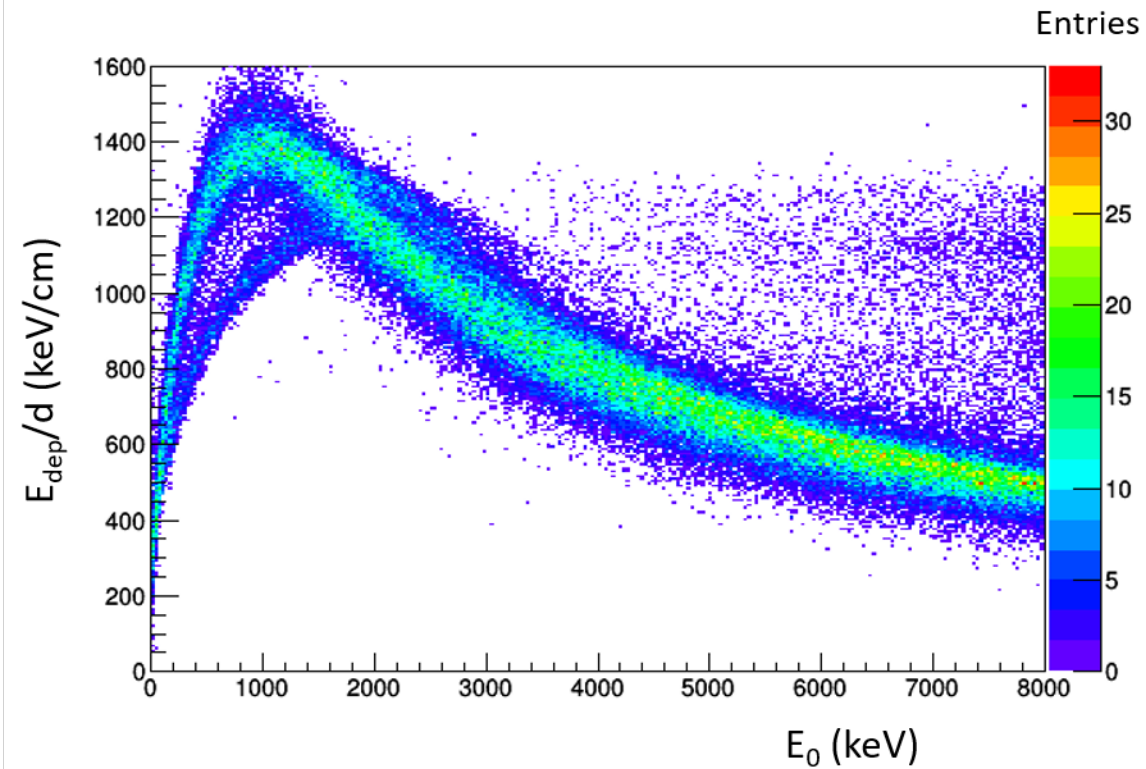
Figure 16: Picture (left) of the uranium ore sample from the Congo (in the form of a “piece”) and the corresponding alpha autoradiograph (right).

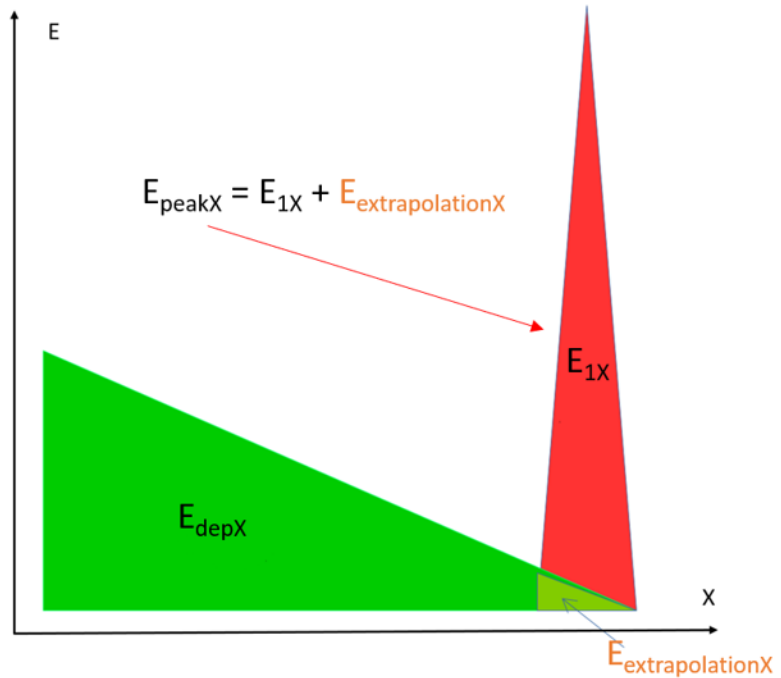
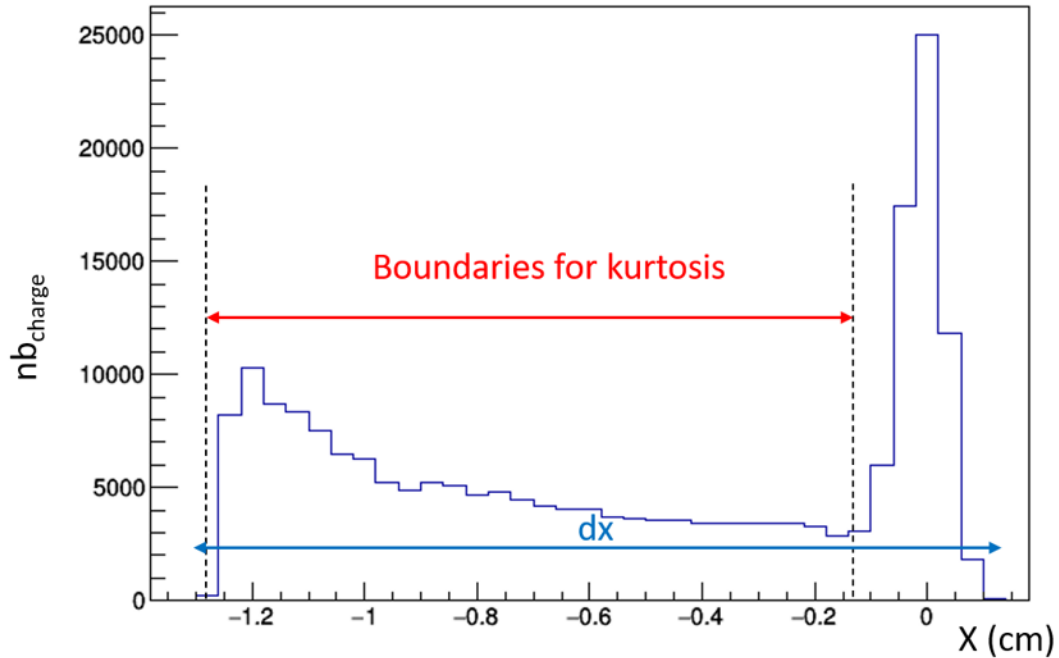
Figure 17: Comparison of the spectrum (divided by its respective internal) of uranium ore obtained with the PIM detector and SA method (in red) with the spectrum obtained from the spectrometry chain after degradation (in blue).

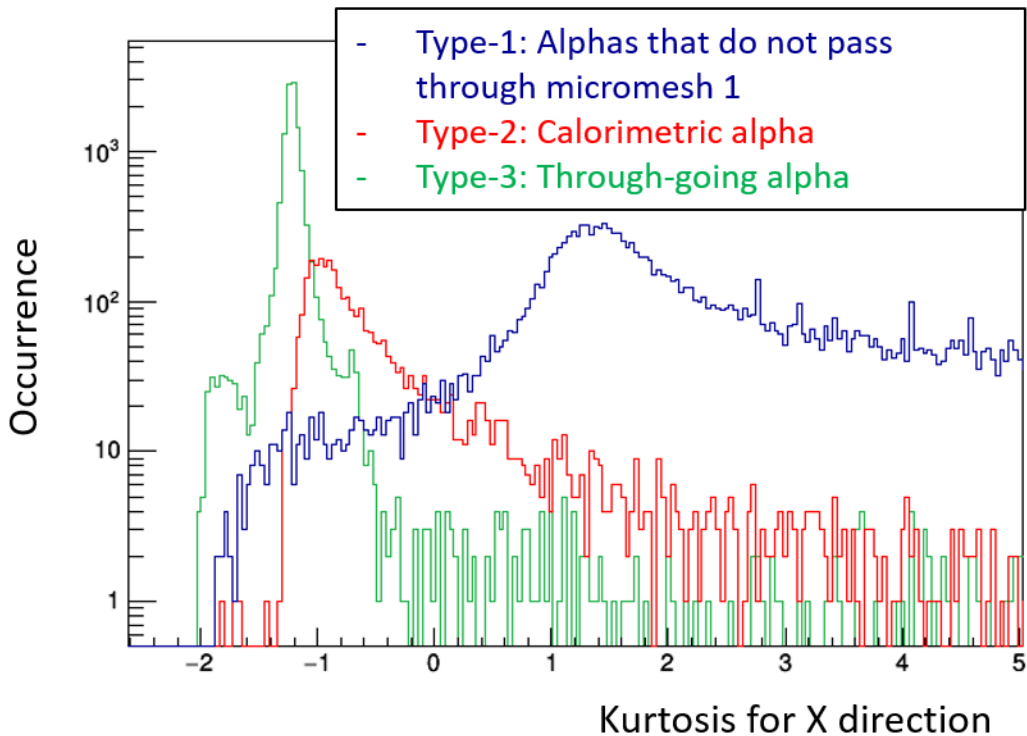


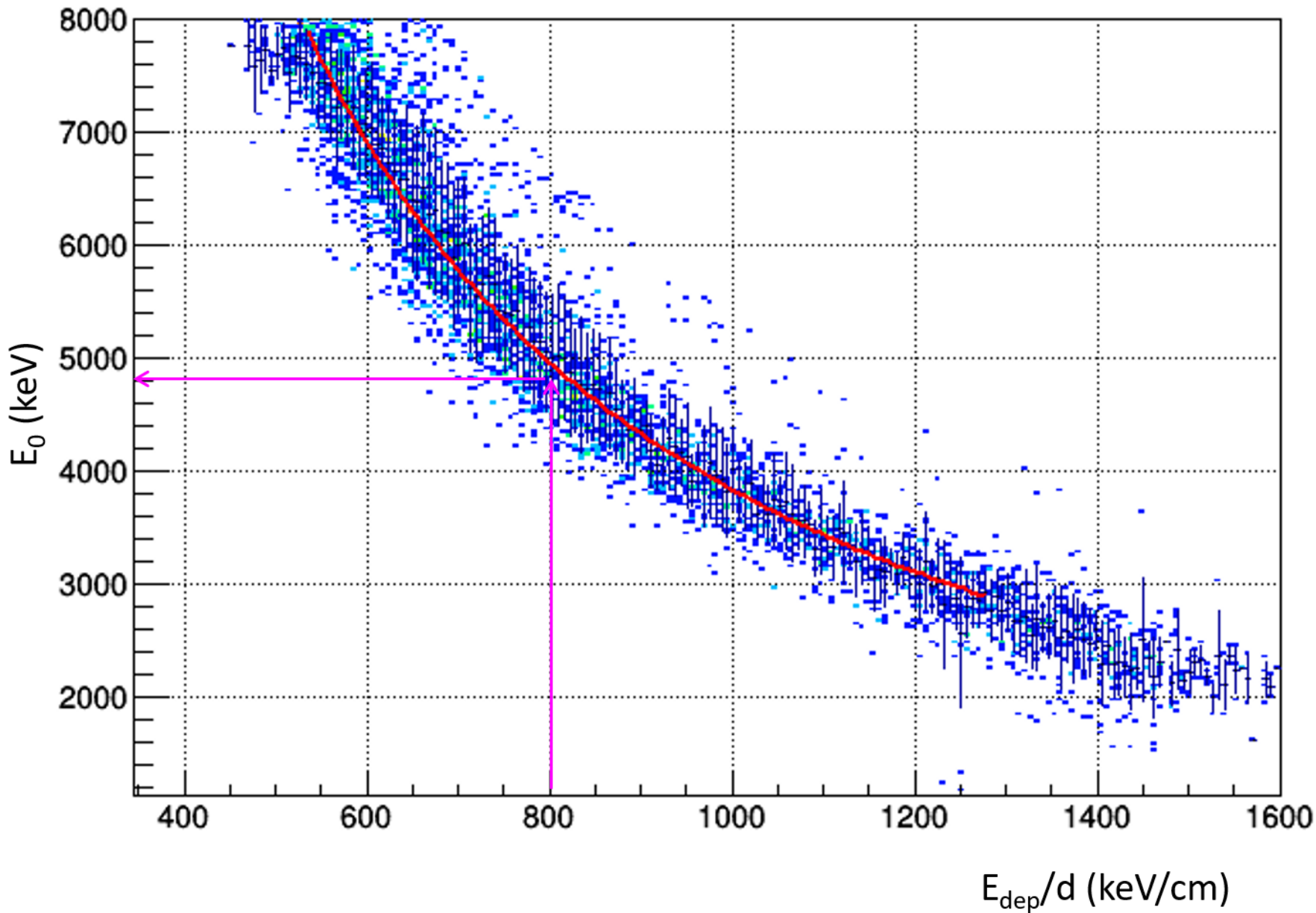


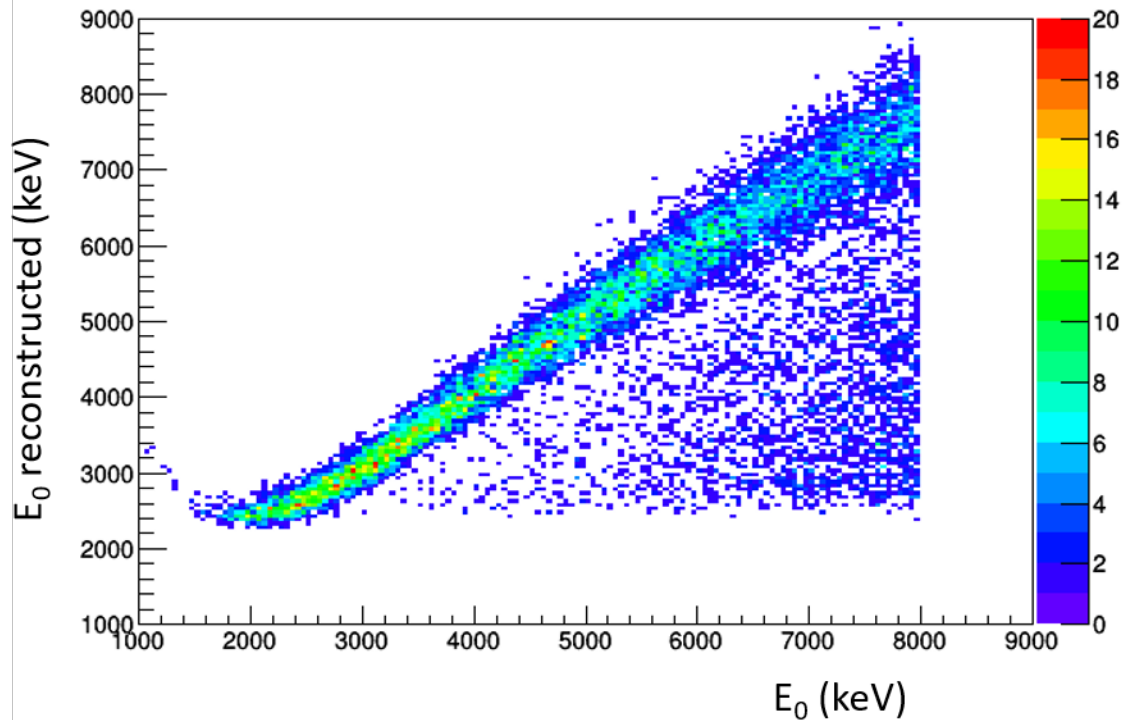


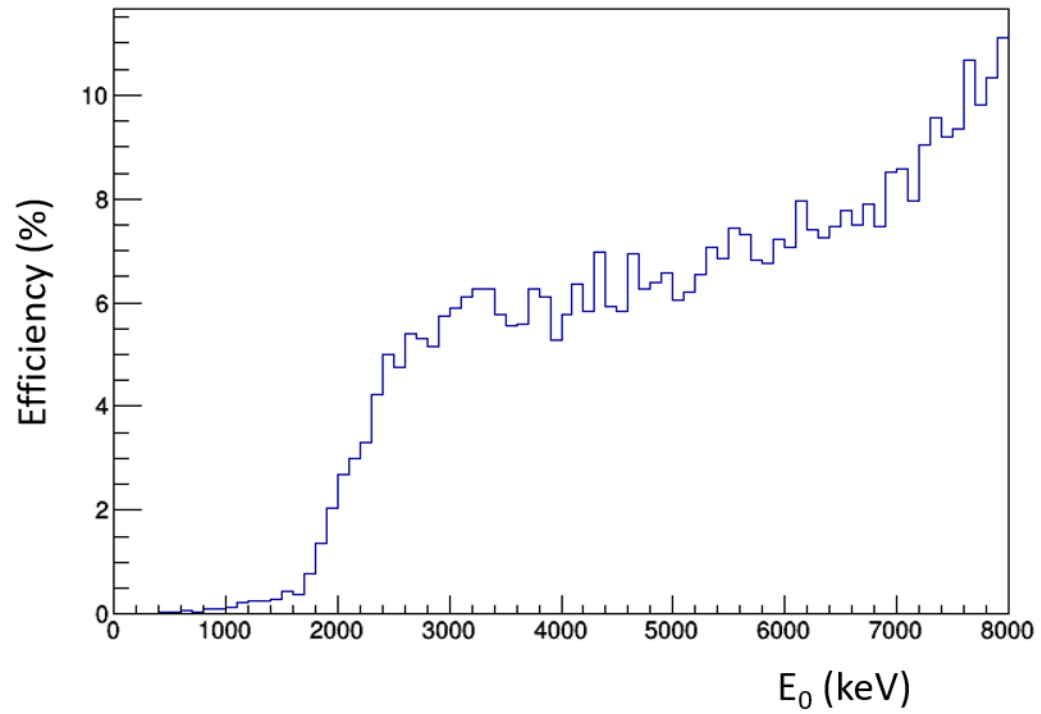
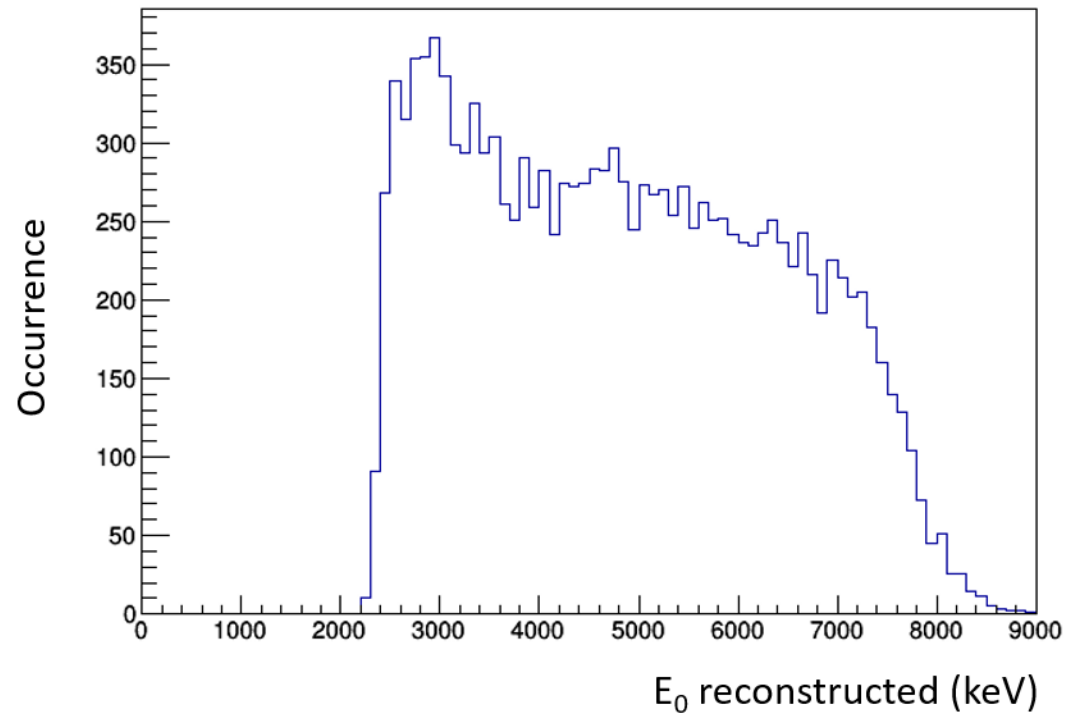


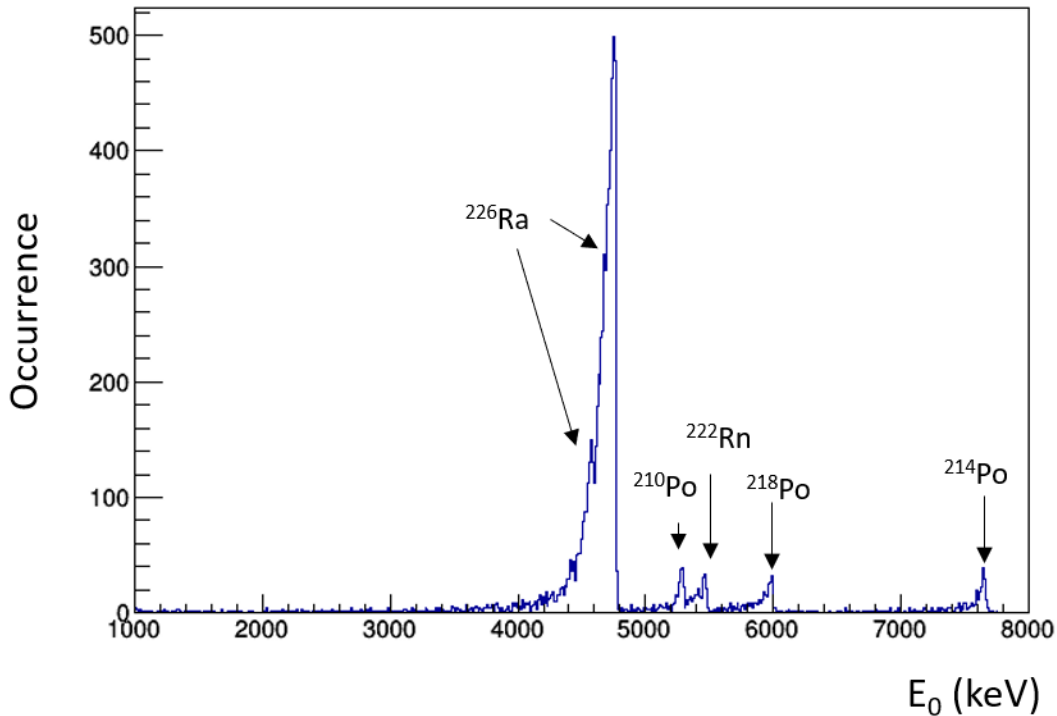


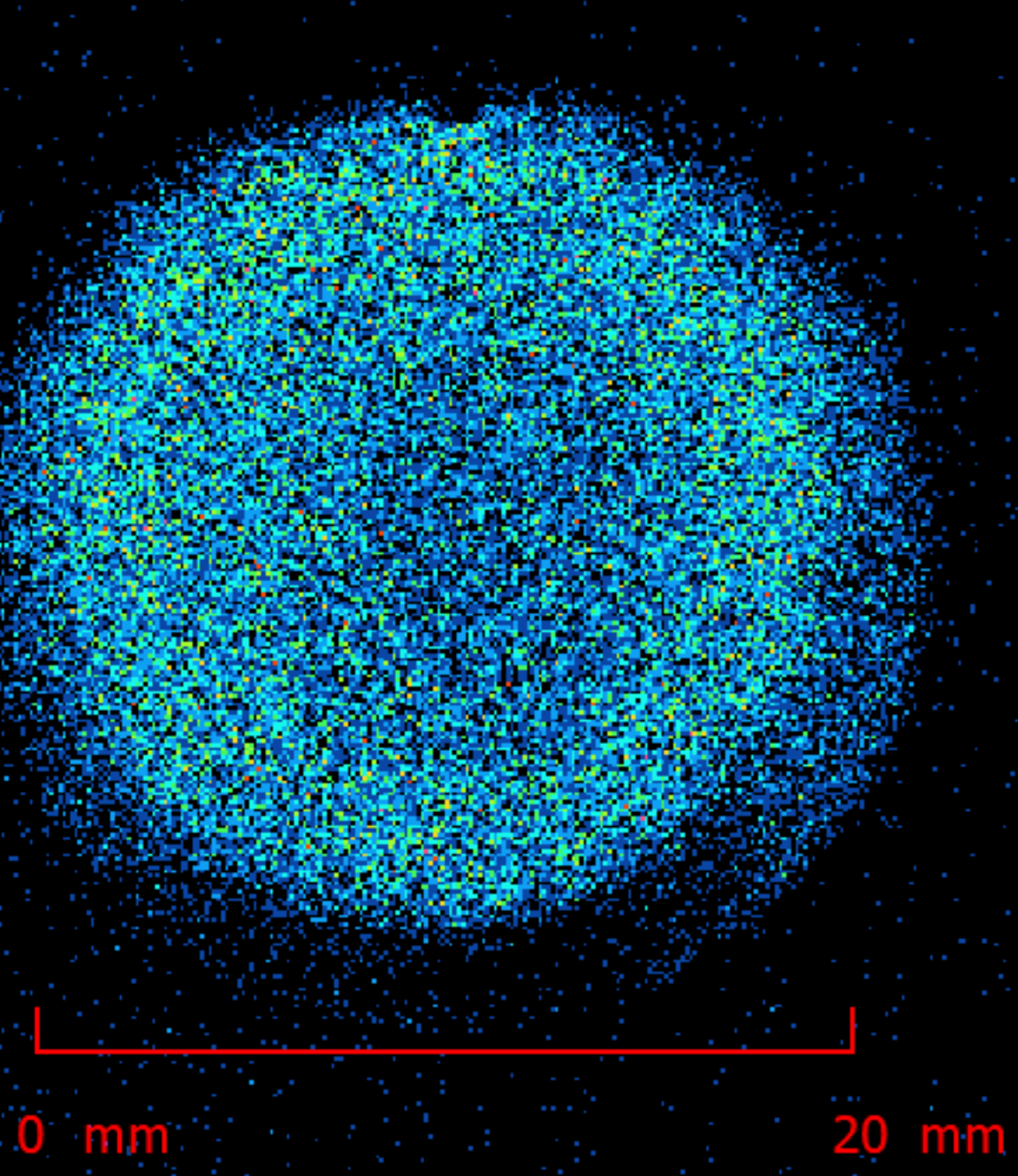


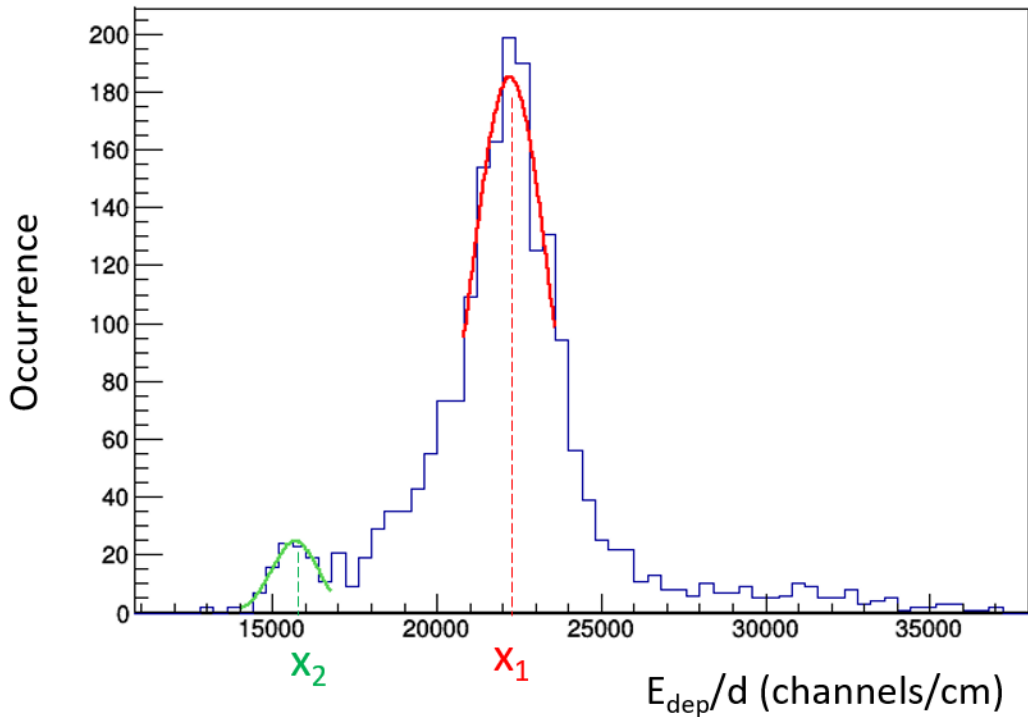


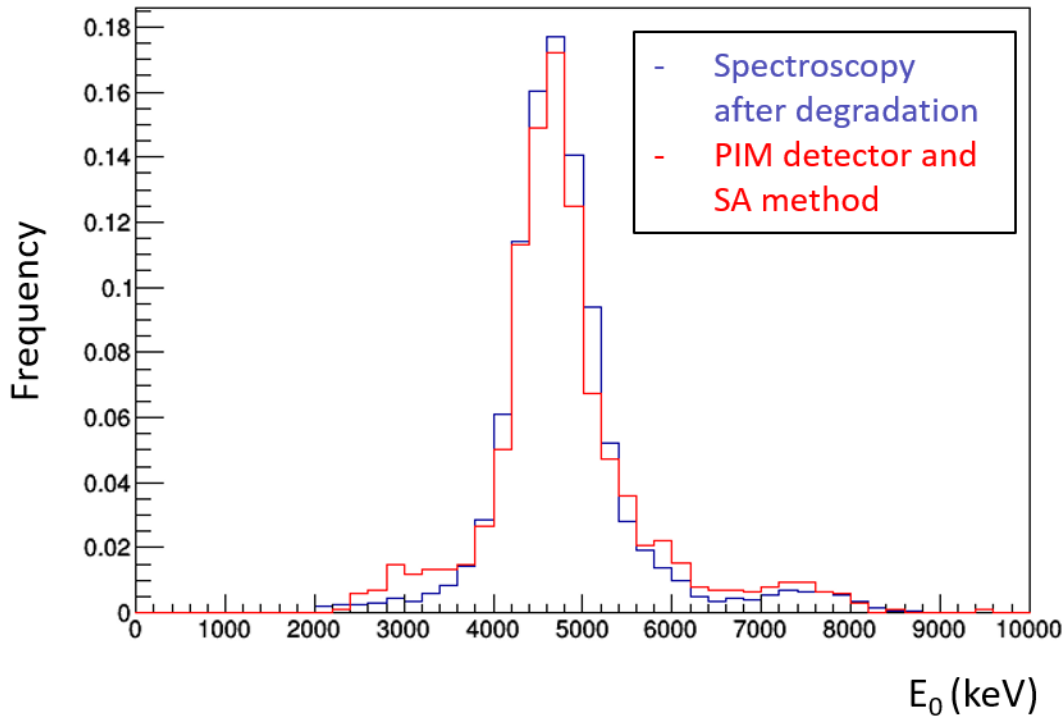


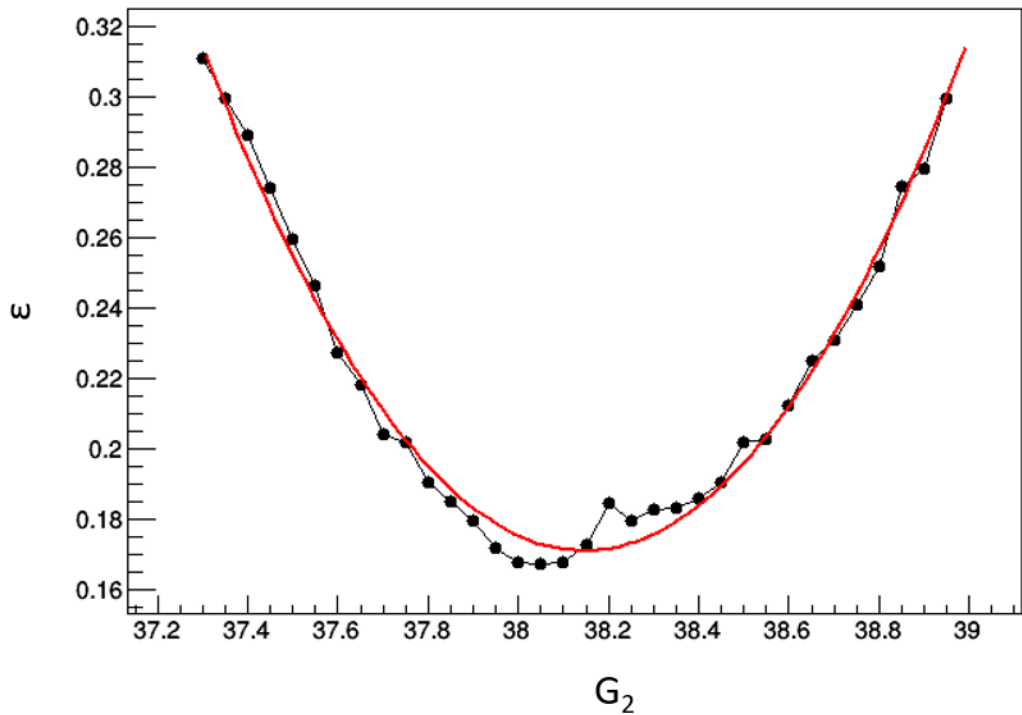


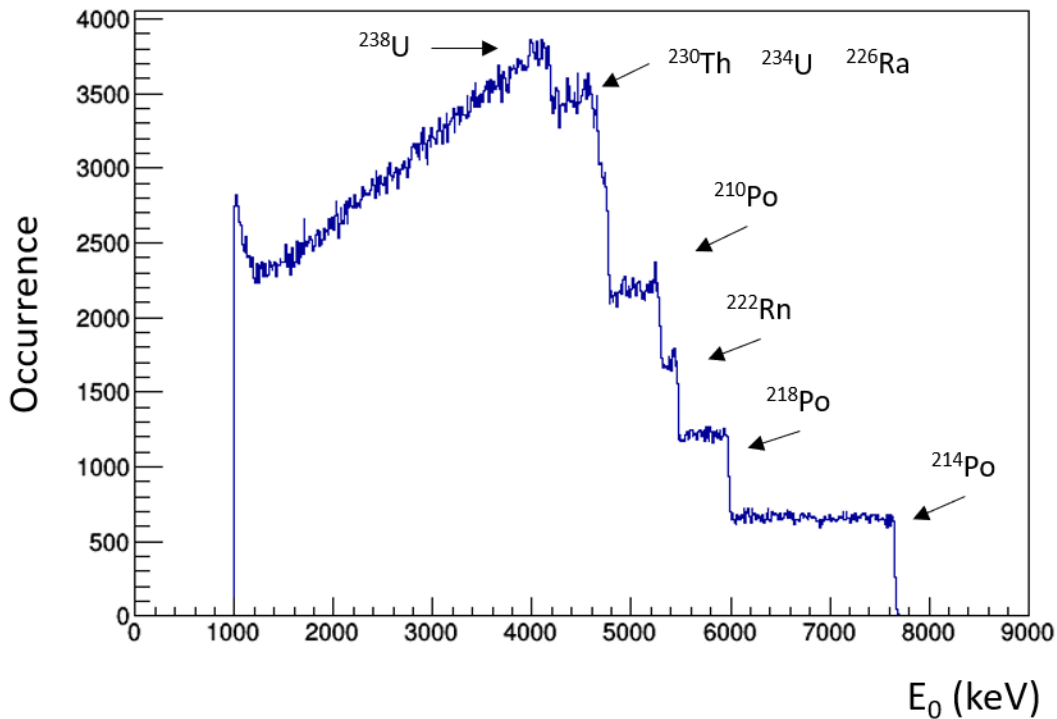


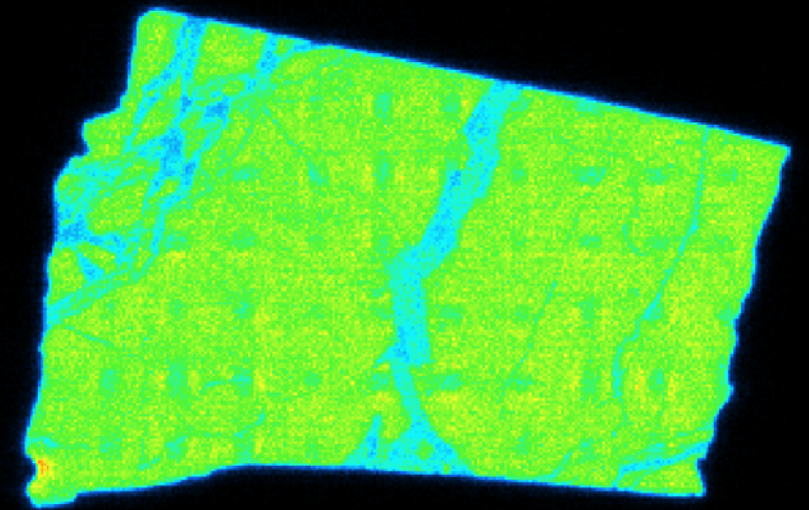
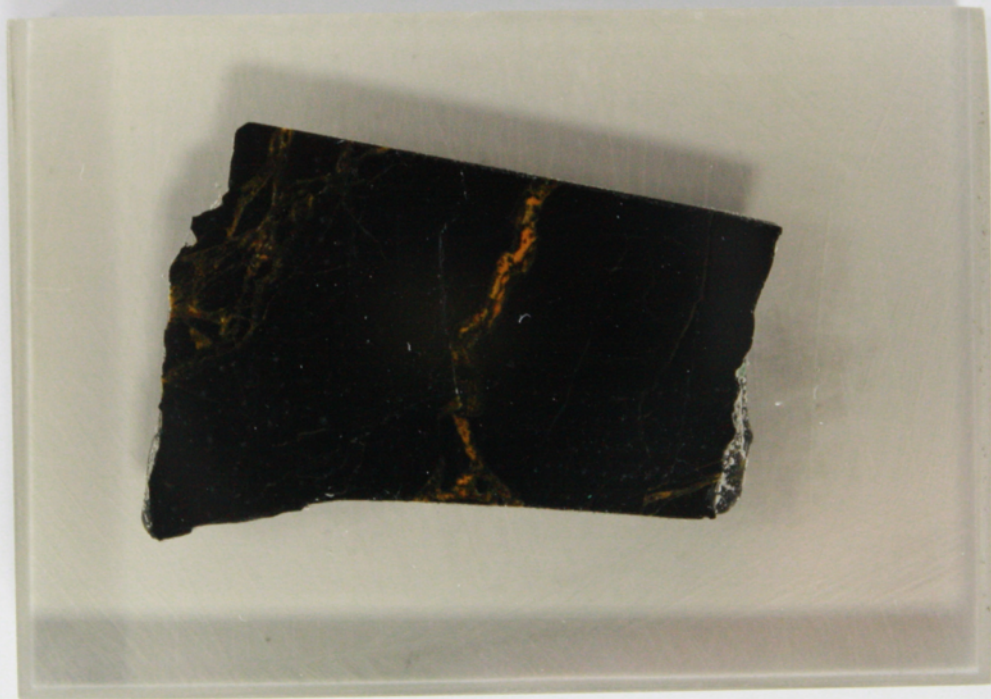












0 mm

25 mm

Counts

700

0

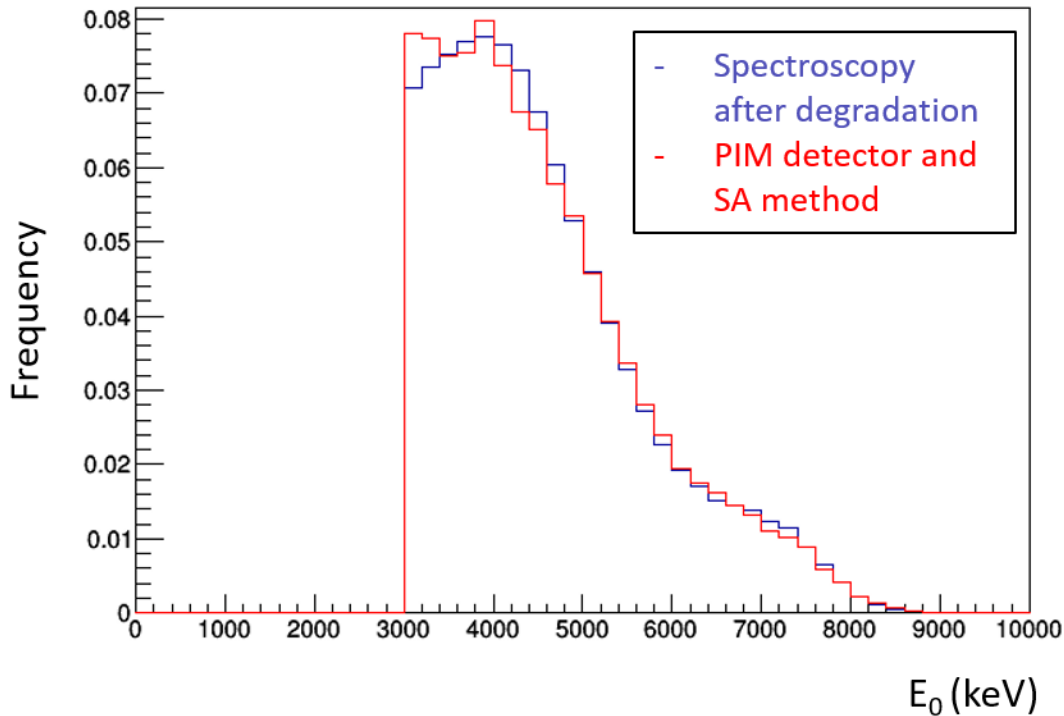


Table 1: Comparative table of important parameters describing the spectroscopic autoradiography devices. These parameters are related to alpha particles detection.

Detector	Sensitive Material technology	Energy Resolution (FWHM)	Spatial Resolution	Active Area	Reference(s)
SiPM	Ce:GAGG Scintillator	13% (5.5 MeV)	600 $\mu\text{m}$	26x26 $\text{mm}^2$	[32]
PSPMT	Stilbene	21.6% (5.5 MeV)	-	20x20 $\text{mm}^2$	[33]
CCD Camera	ZnS(Ag)	56.4 % (5.5 MeV)	390 $\mu\text{m}$	26x26 $\text{mm}^2$	[45]
Timepix	Silicon semi-conductor	0.73% (5.5 MeV)	18 $\mu\text{m}$	14x14 $\text{mm}^2$	[36] [37]
SSNTD	Lexan polycarbonate	6.9% (5.2 MeV)	Several micrometers		[29] [30]
FNTD	$\text{Al}_2\text{O}_3\text{:C,Mg}$ crystals	11.8% (5.49 MeV)	-	70x70 $\mu\text{m}^2$	[41]
Micro-TPC	Gas: $\text{CF}_4$	15.8% (5.3 MeV)	6.8 mm	95x95 $\text{mm}^2$	[44]
Coplanar electrode	Gas: Xe + 0.7% $\text{CH}_4$	1.3% (5.49 MeV)	No position	100 mm	[42]
Coplanar electrode	Gas: Ar + 10% $\text{CH}_4$	2.2% (5.49 MeV)	No position	-	[43]